Optical OTFS Is Capable Of Improving the Bandwidth-, Power- and Energy-Efficiency of Optical OFDM

Chao Xu, *Senior Member, IEEE,* Xiaoyu Zhang, *Member, IEEE,* Periklis Petropoulos, *Member, IEEE,* Shinya Sugiura, *Senior Member, IEEE,* Robert G. Maunder, *Senior Member, IEEE,* Lie-Liang Yang, *Fellow, IEEE,* Zhaocheng Wang, *Fellow, IEEE,* Jinghong Yuan, *Fellow, IEEE,* Harald Haas, *Fellow, IEEE* and Lajos Hanzo* *Life Fellow, IEEE*

***Abstract*—We demonstrate that the proposed optical orthogonal time frequency space (O-OTFS) is capable of improving the bandwidth-/power-/energy-efficiencies of optical orthogonal frequency-division multiplexing (O-OFDM). The bandwidth-efficiency is improved because only a single cyclic prefix (CP) is needed for an entire O-OTFS frame. The power-efficiency is enhanced thanks to the diversity gain achieved by its symplectic finite Fourier transform (SFFT), which also leads to a reduced peak-to-average power ratio (PAPR), hence improving its energy-efficiency. These features are facilitated by the proposed layered asymmetrically clipped O-OTFS (LACO-OTFS), which is capable of removing the direct current (DC) bias while retaining the full optical throughput. Nonetheless, there exists an inherent trade-off, where increasing the O-OTFS frame size leads to a commensurately reduced CP percentage at the cost of an increased PAPR. In order to mitigate this, we propose to perform discrete Fourier transform based spreading (DFT-S) in the delay-Doppler (DD)-domain. Furthermore, we demonstrate that regardless of the choice of domain in which the information is modulated (i.e. O-OFDM/O-OTFS with/without DFT-S), the frequency-selectivity of the quasi-static but dispersive optical channel can always be equalized by single-tap frequency-domain equalization (FDE). Moreover, the channel estimation techniques are conceived to operate in the time-/frequency-/DD-domains for both O-OFDM and O-OTFS. Our simulation results demonstrate that for a multi-user optical wireless system associated with $M = 64$ subcarriers and the OTFS frame length of $N = 64$, LACO-OTFS is capable of achieving a 7 dB power-efficiency gain over LACO-OFDM, where the CP overhead is reduced by a factor of $N = 64$. DFT-S-LACO-OTFS is also capable of providing a 7 dB power-efficiency gain over DFT-S-LACO-OFDM, where the low PAPR of single-carrier transmission is retained.**

***Index Terms*—Optical OFDM, optical OTFS, DCO-OFDM, LACO-OFDM, optical wireless, visible light comunications, wireless near-infrared communications, optical fiber communications, cyclic prefix, peak-to-average power ratio, DFT-spreading, frequency-domain equalization, channel estimation, multi-access.**

C. Xu, X. Zhang, P. Petropoulos, R. G. Maunder L-L. Yang and L. Hanzo are with the School of Electronics and Computer Science, University of Southampton, Southampton SO17 1BJ, UK (e-mail: {cx1g08,xz9g20,pp1,rm,lly,lh}@soton.ac.uk). S. Sugiura is with the Institute of Industrial Science, University of Tokyo, Meguro-ku, Tokyo 153-8505, Japan (e-mail:sugiura@ieee.org). Z. Wang is with the Beijing National Research Center for Infor-mation Science and Technology, Department of Electronic Engineering,Tsinghua University, Beijing 100084, China, and also with the TsinghuaShenzhen International GraduateSchool, Shenzhen 518055, China (e-mail:zcwang@tsinghua.edu.cn). J. Yuan is with School of Electrical Engineering and Telecommunications, University of New South Wales, Sydney, NSW 2052, Australia (e-mail:j.yuan@unsw.edu.au). H. Haas is with the Department of Electronic and Electrical Engineering, University of Strathclyde, Glasgow G1 1RD, UK (e-mail:harald.haas@strath.ac.uk).

The work of S. Sugiura was supported in part by JSPS KAKENHI (Grant Number 22H01481). The work of P. Petropoulos was supported in part by Project REASON, a UK Government funded project under the Future Open Networks Research Challenge (FONRC) sponsored by the Department of Science Innovation and Technology (DSIT) and ESPRC-funded platform TITAN (EP/X04047X/1). L. Hanzo would like to acknowledge the financial support of the Engineering and Physical Sciences Research Council projects EP/W016605/1, EP/X01228X/1 and EP/Y026721/1 as well as of the European Research Council's Advanced Fellow Grant QuantCom (Grant No. 789028)

I. Introduction

Optical orthogonal frequency-division multiplexing (O-OFDM) has experienced a rapid evolution in the recent two decades [1]–[8], owing to its success in mitigating the detrimental frequency selectivity of dispersive optical channels. The optical frequency selectivity is induced by the multipath effect encountered in both visible light comunications (VLC) and wireless near-infrared communications as well as by the chromatic dispersion of optical fiber communications. To elaborate, first of all, by exploiting the illumination capability of light emitting diodes (LEDs), the substantial unlicensed visible light band spanning from about 380 to 780 nm in wavelength can be harnessed by VLC for data transmission. The recent developments on the GaN-based micron-size LEDs have facilitated a modulation bandwidth of 60 MHz for VLC [9]. However, an undesired consequence of increasing the VLC system's bandwidth is that more propagation paths from diffuse, specular and mixed reflections become resolved. Furthermore, on one hand, a relatively high optical transmitter power of about 0.5 Watts has to be dedicated to illuminate objects and surfaces such as the ceilings in indoor VLC scenarios [10], which inevitably results in multipath refelctions. On the other hand, multipath effects are also often observed when multiple line-of-sight (LoS) paths from several LED light sources exist [11]–[13]. The multipath effect in VLC inevitably leads to frequency selectivity that degrades the performance of single-carrier modulation schemes. Secondly, in the absence of the VLC's illumination constraints, the near-infrared band between about 780 nm and 950 nm also constitutes a suitable candidate for the next-generation optical wireless communications [14]–[16]. The near-infrared signals exhibit similar behaviors to visible light, such as the diffuse reflections by light-coloured objects and shiny surfaces. Specifically, non-directed diffuse near-infrared transmission has been shown to be more robust against both the misalignment of directional transceivers and the blockage of LoS. However, this once again leads to increased delay spread that results in severe frequency

selectivity. Thirdly, the phenomenon of chromatic dispersion in optical fiber communications happens when the different frequency components of a light beam arrive at the long-haul destination at slightly different times. A deep fade may be experienced, when these frequency components associated with different phases cancel in the time-domain (TD) [1]. Against this background, O-OFDM is routinely invoked in order to divide the frequency-selective wideband channel into orthogonal non-dispersive parallel subchannels. Thanks to the O-OFDM's subcarrier orthogonality, low-complexity single-tap frequency-domain equalization (FDE) is facilitated for single-symbol demodulation on each subcarrier.

For optical wireless, as well as for multimode fiber and plastic optical fiber systems, the most viable transmission technique is intensity modulation (IM), where the information is carried by the intensity of the emitted optical signal. The most practical receiver technique for IM is direct detection (IM/DD), in which a photodiode (PD) is capable of producing a current that is proportional to the instantaneous power of the received optical signal. The low-complexity IM/DD regime mitigates the cost of generating optical carrier frequencies for down-conversion and supports co-existence with the operational radio frequency (RF) systems. For example, the IM/DD assisted optical wireless systems have promising applications in next-generation space-air-ground integrated networks (SAGINs) [17]–[23], where it is mechanically challenging to deploy large parabolic antennas on small vehicular devices, unmanned aerial vehicles (UAVs) and satellites equipped with RF radios, while the RF interferences to sensitive electronics onboard have to be prevented. The IM/DD based O-OFDM conveys complex-valued quadrature amplitude modulation (QAM) symbols in the frequency-domain (FD), which are mapped to the real- and positive-valued intensity signals in the TD. In order to facilitate this, direct current (DC) biased O-OFDM (DCO-OFDM) [14] was proposed, which relies on the Hermitian symmetry. This dictates that half of the FD symbols are the conjugates of the other half, so that the TD signals become real-valued after inverse fast Fourier transform (IFFT). Furthermore, a DC bias is added to the TD signals before clipping at zero, which produces unipolar intensity signals. DCO-OFDM has been considered as one of the mandatory waveforms in the ongoing optical wireless standardization [12]. However, the choice of the DC bias has substantial impact on the system performance. On one hand, an insufficient DC bias may lead to severe non-linear clipping distortion. On the other hand, excessive DC bias may seriously degrade the system's power-efficiency, because the extra DC bias consumes power without carrying any information. In order to eliminate the DC power consumption, the asymmetrically clipped O-OFDM (ACO-OFDM) [4], [24] arranges odd-indexed subcarriers to obey Hermitian symmetry, while all even-indexed subcarriers are set to zeros. After IFFT, the TD signals become anti-symmetric, which means that all the negative TD signals have a positive counterpart with the same magnitude. As a result, the TD signals can be directly clipped at zero without any information loss, where the clipping distortions fall solely on the even-indexed subcarriers. The drawback of ACO-OFDM is the reduced bandwidth-efficiency due to the inactive subcarriers. We note that similar characteristics associated with the same throughput loss are exhibited both by the pulse amplitude modulation (PAM) based discrete multitone (PAM-DMT) [5] and flip-OFDM [6], where the former only modulates the imaginary parts of all subcarriers, while the latter separately transmits the positive and negative parts of the TD signals. In order to attain the maximum achievable full O-OFDM throughput, the layered ACO-OFDM (LACO-OFDM) [7] modulates all subcarriers layer by layer. For each layer, half of the available subcarriers that are left blank by the lower layers are modulated by appropriately exploiting the Hermitian symmetry and anti-symmetry, as detailed in [25]–[27]. At the receiver, the clipping distortions from the lower layers are removed before demodulating the upper layers with the aid of successive interference cancellation (SIC).

In summary, the O-OFDM schemes facilitate the following benefits. *(I)* Bandwidth-Efficiency: The modulation of the bandwidth-efficient complex-valued QAM is facilitated in the FD, even though the information is conveyed by the intensity rather than by the phase or amplitude in the TD. Moreover, orthogonal multi-access is directly enabled by the trivial bandwidth partition, where multiple users are assigned different subcarriers. *(II)* Power-Efficiency: The inter-symbol interference (ISI) induced by the optical frequency selectivity is mitigated, leading to an improved performance with respect to signal power. *(III)* Energy-Efficiency: Thanks to the quasi-static nature of optical channels, low-complexity single-tap FDE and demodulation can be performed on each subcarrier without encountering inter-carrier interference (ICI). Nonetheless, similar to RF-OFDM, the following O-OFDM deficiencies are also widely recognized. *(i)* Bandwidth-Efficiency: The overhead of cyclic prefix (CP) leads to a bandwidth-efficiency loss. *(ii)* Power-Efficiency: The subcarriers are modulated independently of each other, which fails to attain a key frequency diversity gain. *(iii)* Energy-Efficiency: The IFFT operation imposes a high peak-to-average power ratio (PAPR), which has adverse effects on the optical amplifier in general as well as on the VLC's illumination requirements such as dimming control [28]. In order to improve this, the discrete Fourier transform based spreading (DFT-S) technique is applied to DCO-OFDM, ACO-OFDM and LACO-OFDM in [28]–[30]. On one hand, the DFT-spreading emulates single-carrier transmission that exhibits low PAPR. On the other hand, the DFT-spreading is also capable of distributing the signal energy uniformly over the subcarriers, which results in a beneficial frequency diversity gain. However, in contrast to DFT-S-OFDM for RF systems, the subcarrier allocation required for multi-access becomes challenging in optical DFT-S-OFDM systems, where the local or periodical subcarrier activation patterns [31]–[33] do not comply with the requirement of Hermitian symmetry.

As a further advance, the two-dimensional orthogonal time frequency space (OTFS) modulation [34]–[39] has been intensively investigated in high-Doppler RF systems, owing to its superior performance over OFDM. More explicitly, OTFS modulates the information symbols in the delay-Doppler (DD)-domain instead of the conventional time-frequency (TF)-domain [40]–[42]. On one hand, by invoking the symplectic

finite Fourier transform (SFFT), the OTFS symbols are spread over the entire TF-domain, which improves the diversity gain attained [43]–[45]. On the other hand, the DD-domain channel estimation [37], [38] no longer suffers from time-varying ISI in the TD or from the Doppler-induced ICI in the FD. It was demonstrated in [46] that RF-OTFS is capable of outperforming RF-OFDM even in quasi-static multipath fading channels, which makes OTFS promising also for applications in optics. But one of the major challenges of OTFS is the excessive complexity of data detection, since the modulation dimension in the DD-domain is higher than that of OFDM, while OFDM's SC orthogonality can no longer be relied upon. To mitigate this, the matrix-based minimum mean-squared error (MMSE) equalization techniques of [47], [48] and the message passing (MP) detectors of [49]–[51] were proposed for approaching the optimum performance of the maximum a posteriori (MAP) detector at a reduced complexity.

In contrast to the RF systems, the IM/DD assisted optical systems have real- and positive-valued channel impulse responses (CIRs) in the TD, where the normalized Doppler frequency is often negligible, even in an inter-satellite communication system [17], owing to the short wavelength. Nonetheless, even in quasi-static optical channels, the DCO-OTFS schemes proposed in [52], [53] are shown to outperform their DCO-OFDM counterparts in the following aspects. First of all, a single CP can be shared by an entire DCO-OTFS frame having N O-OFDM symbols. Secondly, DCO-OTFS is capable of achieving an improved diversity performance over DCO-OFDM, which is a benefit of the inverse SFFT (ISFFT) based spreading. Thirdly, the PAPR of DCO-OTFS grows proportionately to the number of O-OFDM symbols N, rather than to the number of OFDM subcarriers M. Nonetheless, optical OTFS (O-OTFS) still faces the following open questions. *(Q-1)* Considering the limited linear optical power-current range, how to conceive a LACO-OTFS that can eliminates the DC power consumption of DCO-OTFS, while retaining the same full IM/DD system throughput? *(Q-2)* There exists an inherent trade-off between bandwidth-efficiency and energy-efficiency for optical OTFS, where increasing the O-OTFS frame size N leads to a favourably reduced CP percentage, but at the cost of an increased PAPR. How to further harness the DFT-S to mitigate the PAPR problem of O-OTFS without increasing the CP overhead? *(Q-3)* Owing to the requirement of Hermitian symmetry, the local or periodical subcarrier assignments routinely used for multi-user RF DFT-S-OFDM are no longer applicable to O-OTFS relying on DFT-S. How to facilitate orthogonal multi-access for LACO-OTFS both with and without DFT-S? *(Q-4)* Considering that optical channels are quasi-static in nature, is it possible for O-OTFS to eliminate the matrix-based MMSE and MP detectors in RF-OTFS? *(Q-5)* For both OFDM and OTFS of RF systems, the classic channel estimation can be performed in TD, FD or DD-domain [37]–[39]. However, the TD clipping leads to spreading in the FD and DD-domain, where the periodic FD pilot insertion and the DD dirac-delta function used for pilot symbols becomes unsustainable. How to facilitate TD/FD/DD-domain channel estimation for O-OTFS?

Against this background, we propose new O-OTFS schemes - namely LACO-OTFS and DFT-S-LACO-OTFS, - which are compared to the state-of-the-art O-OFDM and O-OTFS schemes in Table I. More explicitly, the novel contributions of this work are summarized as follows:

- In answer to *(Q-1)*, a LACO-OTFS scheme is conceived, where the requirements of Hermitian symmetry, TD anti-symmetry and layered successive modulation/demodulation are conceived in the DD-domain. The proposed LACO-OTFS is capable of improving the three-fold efficiencies of the family of O-OFDM schemes in the following aspects:
  - Bandwidth-efficiency is improved due to the fact that only a single CP is needed for an entire LACO-OTFS frame.
  - Power-efficiency is improved due to the diversity gain achieved by the ISFFT spreading.
  - Energy-efficiency is improved due to the fact that the PAPR is reduced, because it only increases with the LACO-OTFS frame size, not with the number of subcarriers.

  We note that this is achieved at the extra cost of ISFFT, which can be implemented as two-dimensional FFT embeded into the hardware architecture [56].
- In answer to *(Q-2)*, a DFT-S-LACO-OTFS scheme is proposed, where DFT spreading is performed along the Doppler axis in the DD-domain, so that the low PAPR of single-carrier transmission is retained, which no longer grows with the O-OTFS frame size.
- In answer to *(Q-3)*, for multi-user LACO-OTFS, the DD symbols can be equally assigned to different users. For DFT-S-LACO-OTFS, a pair of multi-access arrangements are devised. The first one ensures an equal rate for all users, where all symbols are equally assigned to different users before DFT-S. The second one ensures having the minimum PAPR, where each layer is assigned to a single user.
- In answer to *(Q-4)*, we demonstrate that the quasi-static optical channel can always be equalized in the FD by a single-tap FDE, regardless of the choice of domain in which the information is modulated (i.e. TF-domain for O-OFDM or DD-domain for O-OTFS). As a result, for O-OTFS, single-symbol demodulation can be performed in the DD-domain without the computationally complex MMSE or MP detectors of RF OTFS.
- In answer to *(Q-5)*, we propose channel estimation techniques that operate in the TD, FD and DD-domain for both O-OFDM and O-OTFS schemes, where a full O-OFDM symbol or a full O-OTFS frame has to be dedicated to pilot symbols in either the FD or DD-domain, respectively, due to the requirement of Hermitian symmetry and the FD/DD spreading from TD clipping. We demonstrate that DD-domain channel estimation achieves the best performance, albeit at the cost of a higher pilot overhead.

The paper is organized as follows. The proposed LACO-OTFS is presented in Sec. II, where the properties that ensure Hermitian symmetry, TD anti-symmetry and layered

TABLE I: State-of-the-art optical OFDM/OTFS schemes.

	Bandwidth-Efficiency			Power-Efficiency			Energy-Efficiency		
	Full IM/DD Throughput?	Reduced CP?	Orthogonal multi-access?	Remove DC bias?	Diversity gain?	Channel estimation?	Single-carrier PAPR?	Single-tap FDE?	Single-tap demodulation?
DCO-OFDM [14]	√		√					√	√
DFT-S-PAM [28]	√						√	√	√
ACO-OFDM [4]			√	√				√	√
DFT-S-ACO-OFDM [29]				√			√	√	√
PAM-DMT [5]			√	√				√	√
Flip-OFDM [6]			√	√				√	√
LACO-OFDM [7]	√		√	√				√	√
DFT-S-LACO-OFDM [30]	√			√			√	√	√
Machine learning O-OFDM [54], [55]	√			√	√		√		
DCO-OTFS [53]	√	√	√		√				
LACO-OTFS	√	√	√	√	√	√		√	√
DFT-S-LACO-OTFS	√	√	√	√	√	√	√	√	√

TABLE II: Basic O-OFDM and O-OTFS notations.

	TD	FD	DD
Transmitter	$s[n,m]$	$\overline{s}[n,\overline{m}]$	$\widetilde{s}[k,l]$
Fading	$h_{n,m,l}$	$\overline{h}[n,\overline{m}]$	$\widetilde{h}_p \omega_{MN}^{k_p(nM+m-l_p)}$
Receiver	$y[n,m]$	$\overline{y}[n,\overline{m}]$	$\widetilde{y}[k,l]$

successive modulation/demodulation are discussed. The DFT-S is introduced in the DD-domain of Sec. III. Our simulation results are presented in Sec. IV, and our conclusions are offered in Sec. V.

In this work, the wireless efficiencies are considered to be three-fold as categorized in [23], [57]–[60]. Firstly, the bandwidth-efficiency is quantified by the data rate that can be delivered within a given bandwidth. Secondly, the power-efficiency refers to the signal power required for a target performance. Thirdly, the energy-efficiency takes into account the energy consumption for signal processing, which includes the PAPR at the transmitter and the signal detection complexity at the receiver. Furthermore, without loss of generality, OTFS waveforms based on OFDM using rectangular pulses [40], [41], [49] are considered, where the general TD, FD and DD-domain notations are summarized in Table II. An O-OTFS frame consists of N O-OFDM symbols each having M subcarriers, where $0 \leq n \leq N-1$, $0 \leq m \leq M-1$ and $0 \leq \overline{m} \leq M-1$ in Table II represent the O-OFDM symbol index, TD sample index and subcarrier index, respectively. Moreover, $0 \leq l \leq M-1$ and $0 \leq k \leq N-1$ represents the delay and Doppler indices, respectively, while $\{(l_p, k_p)\}_{p=0}^{P-1}$ are the DD indices of the P multipath CIRs. The notations $(\cdot)^*$ and $\exp(\cdot)$ denote the conjugate of a complex number and the natural exponential function, respectively, while we have $\omega_a^b = \exp(j\frac{2\pi b}{a})$. The notations $\Re(\cdot)$ and $\Im(\cdot)$ represent the real and the imaginary parts of a complex number, respectively, while $p(\cdot)$ and $\mathrm{E}(\cdot)$ are the probability and the expectation, respectively.

II. LACO-OTFS

The schematic diagram of the proposed LACO-OTFS transceiver is portrayed by Fig. 1, which will be introduced in detail in this section.

A. Layered Modulation in the DD-Domain

First of all, the proposed LACO-OTFS modulates QAM symbols in J layers along the Doppler axis in the DD-domain. In each layer, a total number of $\frac{N_j}{4}$ QAM symbols

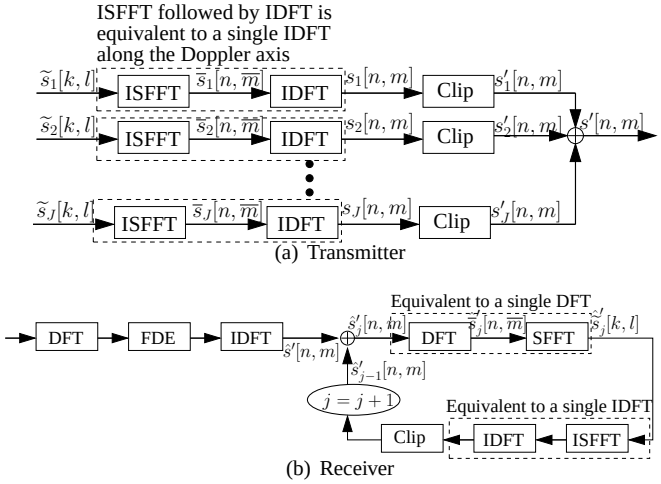

Fig. 1: The schematics of the LACO-OTFS transceiver.

are modulated as $\{x_j[d,l]\}_{d=0}^{\frac{N_j}{4}-1}$, where we have $N_j = \frac{N}{2^{j-1}}$. As presented by Fig. 1(a), the QAM symbols are mapped to J layers as follows:

$$\widetilde{s}_j[k,l] = \begin{cases} x_j[d,l], & k = 2^j d + 2^{j-1} = \frac{N}{N_j}(2d+1) \\ x_j^*[d,l], & k = N - (2^j d + 2^{j-1}) = \frac{N}{N_j}(N_j - (2d+1)) \\ 0, & \text{otherwise} \end{cases}, \tag{1}$$

where we have the layer index $1 \leq j \leq J$ and the data symbol index $0 \leq d \leq \frac{N_j}{4} - 1$. The total number of layers is limited by $J \leq \log_2 N - 1$ because of the constraint of $N_j = \frac{N}{2^{j-1}} \geq 4$. Moreover, the total number of data-carrying symbols is given by $\sum_{j=1}^{J} \frac{N_j}{4} = \sum_{j=1}^{J} \frac{N}{2^{j+1}}$.

Let us consider $N = 64$ as an example. For the first layer ($j = 1$), we have $N_1 = 64$ available positions, but only the odd indices are mapped in order to satisfy the TD anti-symmetry property. The first $\frac{N_1}{4} = 16$ symbols are modulated as $\{\widetilde{s}_1[2d+1,l] = x_1[d,l]\}_{d=0}^{15}$, and the other $\frac{N_1}{4} = 16$ symbols are their conjugates $\{\widetilde{s}_1[64-(2d+1),l] = \widetilde{s}_1^*[2d+1,l]\}_{d=0}^{15}$, aiming for satisfying Hermitian symmetry in the DD-domain. For the second layer ($j = 2$), we have $N_2 = 32$ available positions that have been left blank in the first layer, but once again only half of them are mapped based on the Hermitian symmetry as $\{\widetilde{s}_2[4d+2,l] = x_2[d,l], \widetilde{s}_2[64-(4d+2),l] = \widetilde{s}_2^*[4d+2,l]\}_{d=0}^{7}$. Similarly, for the layers ($j = 3$), ($j = 4$) and ($j = 5$), we have $N_3 = 16$, $N_4 = 8$ and $N_5 = 4$, where the QAM symbols are mapped to $\{\widetilde{s}_3[(8d+4),l] = x_3[d,l], \widetilde{s}_3[64-(8d+4),l] = \widetilde{s}_3^*[8d+4,l]\}_{d=0}^{3}$, $\{\widetilde{s}_4[16d+$

$8,l] = x_4[d,l], \widetilde{s}_4[64-(16d+8),l] = \widetilde{s}_4^*[8d+4,l]\}_{d=0}^{1}$ and $\{\widetilde{s}_5[32d+16,l] = x_5[d,l], \widetilde{s}_5[64-(32d+16),l] = \widetilde{s}_5^*[32d+16,l]\}_{d=0}$, respectively.

B. Transformation from the DD-Domain to the TF-Domain

As shown in Fig. 1(a), the ISFFT is applied to the j-th layer for obtaining the FD OFDM symbols as follows:

$$\overline{s}_j[n,\overline{m}] = \frac{1}{\sqrt{NM}} \sum_{k=0}^{N-1} \sum_{l=0}^{M-1} \widetilde{s}_j[k,l] \omega_N^{nk} \omega_M^{-\overline{m}l}. \tag{2}$$

Then the IDFT is applied to the j-th layer for obtaining TD symbols as follows:

$$\begin{aligned} s_j[n,m] &= \frac{1}{\sqrt{M}} \sum_{\overline{m}=0}^{M-1} \overline{s}_j[n,\overline{m}] \omega_M^{m\overline{m}} \\ &= \frac{1}{\sqrt{N}} \sum_{k=0}^{N-1} \sum_{l=0}^{M-1} \widetilde{s}_j[k,l] \omega_N^{nk} \left(\frac{1}{M} \sum_{\overline{m}=0}^{M-1} \omega_M^{\overline{m}(m-l)} \right) \\ &= \frac{1}{\sqrt{N}} \sum_{k=0}^{N-1} \widetilde{s}_j[k,m] \omega_N^{nk}. \end{aligned} \tag{3}$$

It can be seen that the two steps of the ISFFT applied to the DD symbols followed by the IDFT processing of the OFDM subcarriers become equivalent to a single-step IDFT of the DD symbols along the Doppler axis, as indicated in Fig. 1.

C. Properties of LACO-OTFS in TD Before Clipping

In this section, we introduce the three properties of the TD signals before clipping. Firstly, Property 1 stems from the DD-domain Hermitian symmetry design of (1), which ensures that all TD signals are real-valued.

Property 1 (Hermitian Symmetry): Since half of the DD-domain symbols on each layer are conjugates of the other half, the TD signals obtained from (3) become real-valued as follows:

$$\begin{aligned} s_j[n,m] &= \frac{1}{\sqrt{N}} \sum_{k=0}^{\frac{N}{2}-1} (\widetilde{s}_j[k,m] \omega_N^{nk} + \widetilde{s}_j[N-k,m] \omega_N^{n(N-k)}) \\ &= \frac{1}{\sqrt{N}} \sum_{k=0}^{\frac{N}{2}-1} (\widetilde{s}_j[k,m] \omega_N^{nk} + \widetilde{s}_j^*[k,m] \omega_N^{-nk}) \\ &= \frac{2}{\sqrt{N}} \Re \left(\sum_{k=0}^{\frac{N}{2}-1} (\widetilde{s}_j[k,m] \omega_N^{nk} \right). \end{aligned} \tag{4}$$

Secondly, it can also be observed in the DD-domain mapping of (1) that on each layer, only odd indices $\{2d+1, N_j-(2d+1)\}_{d=0}^{\frac{N_j}{4}-1}$ scaled by $\frac{N}{N_j}$ are modulated. This leads to the following Property 2, which ensures that clipping at zero does not impose any information loss.

Property 2 (Anti-Symmetry): Based on (4), all the negative TD signals on each layer turn out to have a positive counterpart with the same magnitude as follows:

$$\begin{aligned} s_j[n+\frac{N_j}{2},m] &= \frac{2}{\sqrt{N}} \Re \left(\sum_{k=0}^{\frac{N}{2}-1} (\widetilde{s}_j[k,m] \omega_N^{nk} (\omega_N^{\frac{N_j}{2}})^{\frac{N}{N_j}(2d+1)} \right) \\ &= \frac{2}{\sqrt{N}} \Re \left(\sum_{k=0}^{\frac{N}{2}-1} (\widetilde{s}_j[k,m] \omega_N^{nk} (\omega_N^{\frac{N}{2}})^{(2d+1)} \right) \\ &= -s_j[n,m], \end{aligned} \tag{5}$$

where we have $k = \frac{N}{N_j}(2d+1)$ based on (1), and $(\omega_N^{\frac{N}{2}})^{(2d+1)} = -1$ because $(2d+1)$ is odd.

Thirdly, the scaling factor $\frac{N}{N_j}$ applied to the modulation indices $k = \frac{N}{N_j}(2d+1)$ and $k = \frac{N}{N_j}(N_j-(2d+1))$ in (1) results in the following beneficial Property 3 of periodicity. We will show later in Sec. II-E that this property ensures that the clipping noise does not interfere with the lower layers, which is the basis for the proposed successive demodulation of Fig. 1(b).

Property 3 (Periodicity): Based on (4), the TD signals of each layer are periodic with N_j, as follows:

$$\begin{aligned} s_j[\check{n}+\lambda N_j,m]|_{n=\check{n}+\lambda N_j} &= \frac{2}{\sqrt{N}} \Re \left(\sum_{k=0}^{\frac{N}{2}-1} (\widetilde{s}_j[k,m] \omega_N^{\check{n}k} (\omega_N^{\lambda N_j})^{\frac{N}{N_j}(2d+1)} \right) \\ &= \frac{2}{\sqrt{N}} \Re \left(\sum_{k=0}^{\frac{N}{2}-1} (\widetilde{s}_j[k,m] \omega_N^{\check{n}k} (\omega_N^{N})^{\lambda(2d+1)} \right) \\ &= s_j[\check{n},m] \end{aligned} \tag{6}$$

for $n = \check{n}+\lambda N_j$, $0 \le n \le N-1$ and $0 \le \check{n} \le N_j-1$, where we have $(\omega_N^N)^{\lambda(2d+1)} = 1$ for any integer $0 \le \lambda \le \frac{N}{N_j}-1$.

D. Properties of LACO-OTFS in TD After Clipping

The TD signals can now be clipped at zero as:

$$s_j'[n,m] = \begin{cases} s_j[n,m], & \text{if } s_j[n,m] \ge 0 \\ 0, & \text{otherwise} \end{cases}. \tag{7}$$

Thanks to the Property 2 of anti-symmetry, the TD signal of each layer can be clipped at zero without any information loss, which is ensured by the following Property 4 and Property 5 that are extended from Property 2 and Property 3, respectively.

Property 4 (Extended from Property 2): Based on Property 2, a pair of TD samples carry the same information, i.e. we have $s_j[n,m]-s_j[n+\frac{N_j}{2},m] = 2s_j[n,m]$. This property is retained after the clipping operation of (7) with halved power as follows:

$$s_j'[n,m]-s_j'[n+\frac{N_j}{2},m] = s_j[n,m] = \frac{1}{2}(s_j[n,m]-s_j[n+\frac{N_j}{2},m]). \tag{8}$$

Property 5 (Extended from Property 3): Periodicity is also retained after clipping as:

$$s_j'[\check{n}+\lambda N_j,m] = s_j'[\check{n},m], \tag{9}$$

for $0 \le \check{n} \le N_j-1$ and $0 \le \lambda \le \frac{N}{N_j}-1$.

E. Properties of Clipped LACO-OTFS Signal After Converting it Back to the DD-Domain

Let us investigate the properties of the clipped LACO-OTFS signal in the DD-domain, which are the basis for the successive demodulation of Fig. 1(b). Firstly, the DFT on the j-th layer leads to:

$$\overline{s}'_j[n,\overline{m}] = \frac{1}{\sqrt{M}} \sum_{m=0}^{M-1} s'_j[n,m]\omega_M^{-m\overline{m}}. \tag{10}$$

Following this, the SFFT operation on the j-th layer transforms the FD symbols into DD symbols as follows:

$$\begin{aligned}\widetilde{s}'_j[k,l] &= \frac{1}{\sqrt{NM}} \sum_{n=0}^{N-1}\sum_{\overline{m}=0}^{M-1} \overline{s}'_j[n,\overline{m}]\omega_N^{-nk}\omega_M^{\overline{m}l} \\ &= \frac{1}{M\sqrt{N}} \sum_{n=0}^{N-1}\sum_{m=0}^{M-1} s'_j[n,m]\omega_N^{-nk}\sum_{\overline{m}=0}^{M-1}\omega_M^{(l-m)\overline{m}} \\ &= \frac{1}{\sqrt{N}} \sum_{n=0}^{N-1} s'_j[n,l]\omega_N^{-nk}.\end{aligned} \tag{11}$$

Based on (11), we derive the following three properties for data recovery and cross-layer interferences.

Property 6 (Current Layer Recovery): After TD clipping, there is no information loss for any of the layers in the DD-domain. The only change is that of the halved power as follows:

$$\widetilde{s}'_j[k,l] = \frac{1}{\sqrt{N}} \sum_{\lambda=0}^{\frac{N}{N_j}-1}\sum_{\check{n}=0}^{N_j-1} s'_j[\check{n}+\lambda N_j,l]\omega_N^{-\check{n}k}\omega_N^{-\lambda N_j k} \tag{12a}$$

$$= \frac{1}{\sqrt{N}} \sum_{\check{n}=0}^{N_j-1} s'_j[\check{n},l]\omega_N^{-\check{n}k}\sum_{\lambda=0}^{\frac{N}{N_j}-1}\omega_{N/N_j}^{-\lambda k} \tag{12b}$$

$$= \frac{1}{\sqrt{N}} \sum_{\check{n}=0}^{\frac{N_j}{2}-1} s'_j[\check{n},l]\omega_N^{-\check{n}k} + s'_j[\check{n}+\frac{N_j}{2},l]\omega_N^{-\check{n}k}\omega_N^{-\frac{N_j}{2}\frac{N}{N_j}(2d+1)} \tag{12c}$$

$$\times \sum_{\lambda=0}^{\frac{N}{N_j}-1}(\omega_{\frac{N}{N_j}}^{-\frac{N}{N_j}})^{\lambda(2d+1)} \tag{12d}$$

$$= \frac{N}{N_j}\frac{1}{\sqrt{N}} \sum_{\check{n}=0}^{\frac{N_j}{2}-1}\left(s'_j[\check{n},l] - s'_j[\check{n}+\frac{N_j}{2},l]\right)\omega_N^{-\check{n}k} \tag{12e}$$

$$= \frac{1}{2}\widetilde{s}_j[k,l], \tag{12f}$$

where (12b) is obtained based on Property 5. Furthermore, (12d) invokes $k = \frac{N}{N_j}(2d+1)$ in (1), while (12e) is obtained based on $(\omega_N^{-N/2})^{(2d+1)} = -1$ because $(2d+1)$ is odd. Finally, (12f) is obtained based on Property 4.

Property 7 (No Interference to Lower Layers): After TD clipping, the signals on the j-th layer do not impose interference on the $(j-\iota)$-th layer, where $\iota \geq 1$ is a positive integer. More explicitly, at Doppler index $k = \frac{N}{2^\iota N_j}(2d+1)$, we have:

$$\widetilde{s}'_j[k,l] = \frac{1}{\sqrt{N}} \sum_{\lambda=0}^{\frac{N}{2^\iota N_j}-1}\sum_{\check{n}=0}^{2^\iota N_j-1} s'_j[\check{n}+2^\iota\lambda N_j,l]\omega_N^{-\check{n}k}\omega_N^{-2^\iota\lambda N_j k} \tag{13a}$$

$$= \frac{1}{\sqrt{N}} \sum_{\check{n}=0}^{2^\iota N_j-1} s'_j[\check{n},l]\omega_N^{-\check{n}k}\sum_{\lambda=0}^{\frac{N}{2^\iota N_j}-1}\omega_N^{-\lambda N(2d+1)} \tag{13b}$$

$$= \frac{N}{2^\iota N_j}\frac{1}{\sqrt{N}} \sum_{\check{n}=0}^{2^{\iota-1}N_j-1} s'_j[\check{n},l]\omega_N^{-\check{n}k} + s'_j[\check{n}+2^{\iota-1}N_j,l] \tag{13c}$$

$$\times \omega_N^{-\check{n}k}(\omega_N^{-\frac{N}{2}})^{(2d+1)} \tag{13d}$$

$$= 0, \tag{13e}$$

which is obtained from $s'_j[\check{n},l] = s'_j[\check{n}+2^{\iota-1}N_j,l]$ based on Property 5, while we have $(\omega_N^{-\frac{N}{2}})^{(2d+1)} = -1$ because $(2d+1)$ is odd.

Property 8 (Interference to Higher Layers): The clipping noise from the j-th layer will fall on the $(j+\iota)$-th layer, where $\iota \geq 1$ is a positive integer. More explicitly, the DD symbol of (11) associated with the Doppler index $k = \frac{2^\iota N}{N_j}(2d+1)$ is extended as:

$$\widetilde{s}'_j[k,l] = \tag{14a}$$

$$\frac{1}{\sqrt{N}} \sum_{\check{n}=0}^{\frac{N_j}{2}-1}\left\{s'_j[\check{n},l]\omega_N^{-\check{n}k} + s'_j[\check{n}+\frac{N_j}{2},l]\omega_N^{-\check{n}k}\omega_N^{-\frac{N_j}{2}\frac{2^\iota N}{N_j}(2d+1)}\right\} \tag{14b}$$

$$\times \sum_{\lambda=0}^{\frac{N}{N_j}-1}(\omega_{\frac{N}{N_j}}^{-\frac{N}{N_j}})^{\lambda 2^\iota(2d+1)} \tag{14c}$$

$$= \frac{N}{N_j}\frac{1}{\sqrt{N}} \sum_{\check{n}=0}^{\frac{N_j}{2}-1}|s_j[\check{n},l]|\,\omega_N^{-\check{n}k}, \tag{14d}$$

which is obtained from $\omega_N^{-\frac{N_j}{2}\frac{2^\iota N}{N_j}(2d+1)} = (\omega_N^{-N})^{2^{\iota-1}(2d+1)} = 1$ and $s'_j[\check{n},l] + s'_j[\check{n}+\frac{N_j}{2},l] = |s_j[\check{n},l]|$ based on Property 2. Therefore, as shown in Fig. 1(b), upon completing the demodulation of one layer, the LACO-OTFS receiver should re-modulate and demodulated signal and then substract it from the composite received signals in the TD, so that the clipping noise does not contaminate the demodulation of higher layers.

In summary, for the first time in the open literature, the above eight properties are conceived in order to fulfill the requirements of Hermitian symmetry, TD anti-symmetry and layered successive modulation/demodulation in the DD-domain. We note that although the DD-domain Hermitian symmetry was demonstrated for DCO-OTFS in [52], [53], the proposed Property 1 of Hermitian symmetry is conceived for multiple layers of DD-domain modulation, and the proposed Properties 2∼8 further facilitate the first LACO-OTFS scheme

that eliminates the DC power consumption of DCO-OTFS, while retaining the same full IM/DD system throughput.

F. TD Channel Model

As introduced in Sec. I, both optical wireless and optical fiber systems may suffer from frequency selectivity. In this work, we consider the ceiling-bounced model of [15], which is a suitable channel model for both VLC [10] and for the non-directed diffuse near-infrared links [14]. More explicitly, the ceiling-bounced model takes into account a total number of P channel impulse response (CIR) taps associated with delays $\{\tau_p\}_{p=0}^{P-1}$ as follows [15]:

$$h(\tau_p) = \frac{6a^6}{(\tau_p + a)^7}, \tag{15}$$

where the constant a is given by $a = 12\sqrt{\frac{11}{13}}\tau_{\text{RMS}}$, and τ_{RMS} refers to the root mean square delay spread. Therefore, the discrete-time CIR magnitudes are given by $\{h_p = h(\tau_p)|_{\tau_p=\frac{l_p}{M\Delta f}}\}_{p=0}^{P-1}$, where Δf refers to the subcarrier spacing. The power of the LoS $|h_0|^2$ and the power of the NLoS $\sum_{p=1}^{P-1}|h_p|^2$ will be normalized by the Ricean K factor. The delay index of each path h_p is represented by l_p. Explicitly, it was demonstrated in [11], [16], [61] that the Ricean K factor of such an indoor environment may span from -15 dB to 15 dB, and the number of CIR taps may reach $P \geq 10$, where the delay spread is generally within 100 ns. Therefore, a rule-of-thumb is that multipath effects may be observed, when the system bandwidth exceeds 10 MHz.

G. Received Signal in the TD and DD-Domain (OFDM Symbol CP)

If a CP is inserted into each O-OFDM symbol of an O-OTFS frame, the TD received signal is given by:

$$y[n,m] = \sum_{p=0}^{P-1} h_p s'[n, < m - l_p >_M] + v[n,m], \tag{16}$$

where $v[n,m]$ models the additive white Gaussian noise (AWGN) with zero mean and a variance of N_0 [62]. The operation $< m - l_p >_M$ refers to M-tuple circular shifts on m by l_p.

The DFT operation at the receiver transforms the TD signals to the FD symbols as follows:

$$\begin{aligned}\overline{y}[n,\overline{m}] &= \frac{1}{\sqrt{M}}\sum_{m=0}^{M-1} y[n,m]\omega_M^{-m\overline{m}} \\ &= \frac{1}{\sqrt{M}}\sum_{m=0}^{M-1}\sum_{p=0}^{P-1} h_p s'[n, < m - l_p >_M]\omega_M^{-m\overline{m}} \\ &\quad + \frac{1}{\sqrt{M}}\sum_{m=0}^{M-1} v[n,m]\omega_M^{-m\overline{m}} \\ &= \overline{h}_{\overline{m}}\overline{s}'[n,\overline{m}] + \overline{v}[n,\overline{m}],\end{aligned} \tag{17}$$

where the channel's frequency response (CFR) is given by $\overline{h}_{\overline{m}} = \sum_{p=0}^{P-1} h_p \omega_M^{-l_p\overline{m}}$.

Finally, the SFFT transforms the FD symbols to the DD symbols as follows:

$$\begin{aligned}\widetilde{y}[k,l] &= \frac{1}{\sqrt{MN}}\sum_{n=0}^{N-1}\sum_{\overline{m}=0}^{M-1}\overline{y}[n,\overline{m}]\omega_N^{-nk}\omega_M^{\overline{m}l} = \frac{1}{\sqrt{N}}\sum_{n=0}^{N-1} y[n,l]\omega_N^{-nk} \\ &= \frac{1}{\sqrt{N}}\sum_{n=0}^{N-1}\sum_{p=0}^{P-1} h_p s'[n, < l - l_p >_M]\omega_N^{-nk} + \widetilde{v}[k,l] \\ &= \frac{1}{N}\sum_{p=0}^{P-1} h_p \sum_{k'=0}^{N-1}\widetilde{s}'[k', < l - l_p >_M]\sum_{n=0}^{N-1}\omega_N^{n(k'-k)} + \widetilde{v}[k,l] \\ &= \sum_{p=0}^{P-1} h_p \widetilde{s}'[k, < l - l_p >_M] + \widetilde{v}[k,l].\end{aligned} \tag{18}$$

H. Received Signal in the TD and DD-Domain (OTFS Frame CP)

If a single CP is inserted at the beginning of an O-OTFS frame, the TD received signal of (16) becomes:

$$y[nM+m] = \sum_{p=0}^{P-1} h_p s'[< nM + m - l_p >_{NM}] + v[nM+m], \tag{19}$$

where the period of the circular convolution is extended from M to MN. As a result, following the DFT and SFFT operations at the receiver, the DD received signals of (18) become:

$$\begin{aligned}\widetilde{y}[k,l] &= \frac{1}{\sqrt{N}}\sum_{n=0}^{N-1} y[n,l]\omega_N^{-nk} \\ &= \frac{1}{\sqrt{N}}\sum_{n=0}^{N-1}\sum_{p=0}^{P-1} h_p s'[< nM + l - l_p >_{NM}]\omega_N^{-nk} + \widetilde{v}[k,l],\end{aligned} \tag{20}$$

where the TD symbols are in the form of:

$$s'[< nM+l-l_p >_{NM}] = \begin{cases} s'[n, < l - l_p >_M], & l \geq l_p \\ s'[n-1, < l - l_p >_M], & l < l_p, n > 0 \\ s'[N-1, < l - l_p >_M], & l < l_p, n = 0 \end{cases}. \tag{21}$$

Specifically, for the case of $l < l_p$, (21) becomes:

$$\begin{aligned}\widetilde{y}[k,l] &= \frac{1}{\sqrt{N}}\sum_{p=0}^{P-1} h_p s'[N-1, < l - l_p >_M] \\ &\quad + \frac{1}{\sqrt{N}}\sum_{n=1}^{N-1}\sum_{p=0}^{P-1} h_p s'[n-1, < l - l_p >_M]\omega_N^{-nk} + \widetilde{v}[k,l] \\ &= \frac{1}{\sqrt{N}}\sum_{n=0}^{N-1}\sum_{p=0}^{P-1} h_p \omega_N^{-k} s'[n, < l - l_p >_M]\omega_N^{-nk} + \widetilde{v}[k,l].\end{aligned} \tag{22}$$

Therefore, the DD-domain input-output relationship is generalized by:

$$\widetilde{y}[k,l] = \sum_{p=0}^{P-1} h_p \mathcal{T}(k,l,l_p)\widetilde{s}'[k, < l - l_p >_M] + \widetilde{v}[k,l], \tag{23}$$

where the delay-dependent phase is given by:

$$\mathcal{T}(k,l,l_p) = \begin{cases} 1, & l \geq l_p \\ \omega_N^{-k}, & l < l_p \end{cases} . \quad (24)$$

I. Single-Tap FDE and Demodulation

The time-invariant optical channel does not impose inter-carrier interference in the FD. Hence regardless of the choice of domain for data modulation, the optical channel can always be equalized in the FD as follows:

$$\hat{\overset{\vee}{s}}'[n,\overline{m}] = \overline{y}[n,\overline{m}]/\overline{h}_{\overline{m}}, \quad (25)$$

where $\overline{y}[n,\overline{m}]$ and $\overline{h}_{\overline{m}}$ are given by (17). For OTFS frame-based CP, the FDE is given by:

$$\hat{\overset{\vee}{s}}'[nM+\overline{m}] = \overline{y}[nM+\overline{m}]/\overline{h}_{\overline{m}}, \quad (26)$$

where $\overline{y}[nM+\overline{m}]$ and $\overline{h}_{\overline{m}}$ are also obtained following (17) using MN-point DFT. Upon obtaining the equalized TD signals $\hat{s}'[n,m]$ by M-point IDFT and MN-point IDFT for symbol CP and frame CP, respectively, the DD-domain demodulation can be performed layer-by-layer based on Property 6, as portrayed by Fig. 1(b). When a layer is demodulated, the associated TD signals $\hat{s}'_j[n,m]$ have to be substracted from $\hat{s}'[n,m]$, so that the current layer does not impose interference upon the higher layers.

J. Simplification for LACO-OTFS Modulation

The DD-domain modulation of (1) may be simplified to the following form:

$$\overset{\vee}{\overset{\vee}{s}}_j[\check{k},l] = \begin{cases} x_j[d,l], & \check{k} = 2d+1 \\ x_j^*[d,l], & \check{k} = N_j-(2d+1) \\ 0, & \check{k} \text{ is even} \end{cases} , \quad (27)$$

where we have $0 \leq \check{k} \leq N_j - 1$, while the other parameters are the same as given in (1). As a result, the ISFFT of (2) may have a reduced dimension on the Doppler axis as:

$$\overset{\vee}{\overset{\vee}{s}}_j[\check{n},\overline{m}] = \frac{1}{\sqrt{N_j M}} \sum_{\check{k}=0}^{N_j-1} \sum_{l=0}^{M-1} \overset{\vee}{\overset{\vee}{s}}_j[\check{k},l] \omega_{N_j}^{\check{n}\check{k}} \omega_M^{-\overline{m}l}, \quad (28)$$

where we have $0 \leq \check{n} \leq N_j - 1$. Following this, the IDFT operation may proceed as follows:

$$\begin{aligned} \check{s}_j[\check{n},m] &= \frac{1}{\sqrt{M}} \sum_{\overline{m}=0}^{M-1} \overset{\vee}{\overset{\vee}{s}}_j[\check{n},\overline{m}] \omega_M^{m\overline{m}} \\ &= \frac{1}{\sqrt{N_j}} \sum_{\check{k}=0}^{N_j-1} \sum_{l=0}^{M-1} \overset{\vee}{\overset{\vee}{s}}_j[\check{k},l] \omega_{N_j}^{\check{n}\check{k}} \left(\frac{1}{M} \sum_{\overline{m}=0}^{M-1} \omega_M^{\overline{m}(m-l)} \right) \\ &= \frac{1}{\sqrt{N_j}} \sum_{\check{k}=0}^{N_j-1} \overset{\vee}{\overset{\vee}{s}}_j[\check{k},m] \omega_{N_j}^{\check{n}\check{k}} \\ &= \frac{2}{\sqrt{N_j}} \Re \left(\sum_{d=0}^{\frac{N_j}{4}-1} x_j[d,m] \omega_{N_j}^{\check{n}(2d+1)} \right) . \end{aligned} \quad (29)$$

Based on (27) and (4), since the original TD samples of LACO-OTFS are given by $s_j[n,m] = \frac{2}{\sqrt{N}} \Re \left(\sum_{d=0}^{\frac{N_j}{4}-1} x_j[d,m] \omega_{N_j}^{n(2d+1)} \right)$, the following power amplification is required for the simplified modulation in the TD:

$$s_j[n,m] = \sqrt{\frac{N_j}{N}} \check{s}_j[< n >_{N_j}, m]. \quad (30)$$

III. DFT-S-LACO-OTFS

In this section, we propose the DFT-S-LACO-OTFS scheme, which ensures single-carrier PAPR transmission, while retaining the single frame-based CP design.

A. Design Goals

As demonstrated in Sec. II-B, the combination of ISFFT and IDFT becomes equivalent to performing a single IDFT applied to the DD symbols along the Doppler axis. Therefore, in order to retain a single-carrier PAPR, we propose to perform DFT-S along the Doppler axis in the DD-domain. The OFDM-based structure is retained for the sake of using single-step FDE and demodulation. The modulation before DFT-S should aim to fulfill Properties 1-3 for the TD signal. This means that the TD signals on the j-th layer $\{\{s_j[n,m]\}_{n=0}^{N-1}\}_{m=0}^{M-1}$ have to be real-valued PAM symbols for satisfying the Hermitian symmetry of Property 1. They have to satisfy $\{s_j[n+\frac{N_j}{2},m] = -s_j[n,m]\}_{n=0}^{\frac{N_j}{2}-1}$ and $\{s_j[n+N_j,m] = s_j[n,m]\}_{n=0}^{N_j-1}$ for satisfying the anti-symmetry of Property 2 and the periodicity of Property 3, respectively.

B. Multi-Access Modulation Before DFTS

In this section, a pair of multi-access arrangements are conceived for DFT-S-LACO-OTFS. For the Equal-Rate arrangement, a total of $\frac{N_j}{2}$ PAM symbols mapped to each layer are equally assigned to U users as:

$$\check{s}_j[\check{d},l] = \begin{cases} x_j[d,l], & \check{d} = u\frac{N_j}{2U} + d \\ -x_j[d,l], & \check{d} = u\frac{N_j}{2U} + d + \frac{N_j}{2} \\ 0, & \text{otherwise} \end{cases} , \quad (31)$$

where the user index is given by $0 \leq u \leq U-1$, the modulated symbol index for each user is within the range of $0 \leq d \leq \frac{N_j}{2U} - 1$, and the overall symbol index is $0 \leq \check{d} \leq N_j - 1$. The other parameters are the same as defined for (27). The total number of modulated symbols assigned to each user is given by $\sum_{j=1}^{J} \frac{N_j}{2U} = \sum_{j=1}^{J} \frac{N}{2^j U}$. The number of layers is limited by $J \leq \log_2 \frac{N}{U}$, which is obtained from $\frac{N}{2^J U} \geq 1$. The maximum number of users is limited by the number of symbols in the first layer, i.e. we have $U \leq \frac{N}{2}$.

Alternatively, for the Layer-User arrangement, one layer of $\frac{N_j}{2}$ PAM symbols is assigned to one user as follows:

$$\check{s}_j[\check{d},l] = \begin{cases} x_j[d,l], & \check{d} = d \\ -x_j[d,l], & \check{d} = d + \frac{N_j}{2} \\ 0, & \text{otherwise} \end{cases} , \quad (32)$$

where we have $0 \leq d \leq \frac{N_j}{2} - 1$ and $0 \leq \check{d} \leq N_j - 1$. As a result, the total number of modulated symbols assigned to the

TABLE III: DFT-S-LACO-OTFS Parameters.

	Equal-Rate	Layer-User
Number of symbols per user	$\sum_{j=1}^{J} \frac{N_j}{2U} = \sum_{j=1}^{J} \frac{N}{2^j U}$	$\frac{N_j}{2} = \frac{N}{2^j}$
Maximum number of layers	$J \leq \log_2 \frac{N}{U}$	$J \leq \log_2 N$
Maximum number of users	$U \leq \frac{N}{2}$	$U \leq J$
PAPR	Incrasing with $J \leq \log_2 \frac{N}{U}$	Single-carrier

$(u = j)$-th user is given by $\frac{N_j}{2} = \frac{N}{2^j}$. The number of layers is limited by $J \leq \log_2 N$, which is obtained from $\frac{N}{2^j} \geq 1$. The maximum number of users is limited by the number of layers, i.e. we have $U \leq J$.

The parameters of the Equal-Rate and Layer-User arrangements are summarized in Table III. First of all, the Equal-Rate arrangement has the same throughput for all users, while the Layer-User method has a decreasing throughput as the layer/user index $u = j$ increases. Secondly, the Equal-Rate method can support fewer layers than Layer-User, owing to the fact that the number of modulated symbols of legitimate layers has to be equal to or higher than the number of users for Equal-Rate, i.e. $\frac{N}{2^j U} \geq 1$. Thirdly, the Equal-Rate method can support more users, as the number of users of the Layer-User arrangement is limited by the number of layers. Finally, we will demonstrate in Sec. IV-E that the PAPR of the Equal-Rate arrangement grows with $J \leq \log_2 \frac{N}{U}$, which is already substantially lower than the PAPR of O-OTFS without DFT-S that grows with N. Furthermore, the Layer-User arrangement achieves single-carrier PAPR, owing to the fact that the DFT-S is applied to each layer/user.

C. DD-Domain Mapping

Following the modulation, N_j-point DFT spreading is performed in the DD-domain as follows:

$$\check{\tilde{s}}_j[\check{k}, l] = \frac{1}{\sqrt{N_j}} \sum_{\check{d}=0}^{N_j-1} \check{s}_j[\check{d}, l] \omega_{N_j}^{-\check{k}\check{d}}. \tag{33}$$

Therefore, the DD-domain Hermitian symmetry property of (27), which requires that half of the DD symbols are conjugate versions of the other half, is retained:

$$\check{\tilde{s}}_j[N_j - \check{k}, l] = \frac{1}{\sqrt{N_j}} \sum_{\check{d}=0}^{N_j-1} \check{s}_j[\check{d}, l] \omega_{N_j}^{(N_j-\check{k})\check{d}} = \check{\tilde{s}}_j^*[\check{k}, l], \tag{34}$$

where we have $\check{s}_j^*[\check{d}, l] = \check{s}_j[\check{d}, l]$, because they are real-valued PAM symbols.

Furthermore, the DD-domain property of (27) that $\check{\tilde{s}}_j[\check{k}, l] = 0$ for even indices $\check{k}$ is also retained:

$$\check{\tilde{s}}_j[\check{k}, l] = \frac{1}{\sqrt{N_j}} \sum_{\check{d}=0}^{\frac{N_j}{2}-1} \check{s}_j[\check{d}, l] \omega_{N_j}^{-\check{k}\check{d}} + \check{s}_j[\check{d} + \frac{N_j}{2}, l] \omega_{N_j}^{-\check{k}\check{d}} (\omega_{N_j}^{-\frac{N_j}{2}})^{\check{k}}, \tag{35}$$

where we have $\check{s}_j[\check{d} + \frac{N_j}{2}, l] = -\check{s}_j[\check{d}, l]$ and $\omega_{N_j}^{-\frac{N_j}{2}} = -1$.

In order to restore the same dimension as that of the LACO-OTFS of Sec. II-B, zeros are inserted in the DD-domain as follows:

$$\widetilde{s}_j[k, l] = \begin{cases} \check{\tilde{s}}_j[\check{k}, l] & k = \frac{N}{N_j}\check{k} \\ 0, & \text{otherwise} \end{cases}. \tag{36}$$

As a result, the conjugate symbols and zeros are located at the same positions as (1), where

$$\widetilde{s}_j[N - k, l] = \widetilde{s}_j[\frac{N}{N_j}(N_j - \check{k}), l] = \check{\tilde{s}}_j[N_j - \check{k}, l] = \check{\tilde{s}}_j^*[\check{k}, l]. \tag{37}$$

D. Retaining TD Properties

Following the ISFFT and IDFT operations of Sec. II-B, the TD signals are generated by:

$$\begin{aligned} s_j[n, m] &= \frac{1}{\sqrt{N}} \sum_{k=0}^{N-1} \widetilde{s}_j[k, m] \omega_N^{nk} = \frac{1}{\sqrt{N}} \sum_{\check{k}=0}^{N_j-1} \check{\tilde{s}}_j[\check{k}, m] \omega_{N_j}^{n\check{k}} \\ &= \frac{1}{\sqrt{N N_j}} \sum_{\check{d}=0}^{N_j-1} \check{s}_j[\check{d}, m] \sum_{\check{k}=0}^{N_j-1} \omega_{N_j}^{(n-\check{d})\check{k}} \\ &= \sqrt{\frac{N_j}{N}} \check{s}_j[< n >_{N_j}, m]. \end{aligned} \tag{38}$$

First of all, (38) evidences that low-PAPR single-carrier transmission is ensured for each layer, where the PAM symbols are modulated either based on Equal-Rate or Layer-User arrangements. Secondly, the real-valued Property 1 is also satisfied by the PAM modulation. Thirdly, the anti-symmetry of Property 2 is ensured by the Equal-Rate or Layer-User mapping of (31) and (32), respectively. Fourthly, the periodicity Property 3 is ensured by the DD mapping of (36). Finally, the power scaling of (30) is avoided, thanks to the DD mapping of (36).

IV. Performance Results

In this section, the performance results of the various OFDM and OTFS schemes discussed in this work are presented in terms of the bandwidth-efficiency with respect to CP overhead and throughput R, of the power-efficiency with respect to SNR required for meeting the target BER as well as of the energy-efficiency with respect to the PAPR.

A. Major Benchmarks and General Parameters

We take into account all existing optical OFDM and optical OTFS schemes as benchmarks. Firstly, DCO-OFDM [14] modulates QAM symbols in the FD as follows:

$$\overline{s}[n, \overline{m}] = \begin{cases} \overline{s}[n, \overline{m}], & 1 \leq \overline{m} \leq \frac{M}{2} - 1 \\ \overline{s}^*[n, M - \overline{m}], & \frac{M}{2} + 1 \leq \overline{m} \leq M - 1 \\ 0, & \text{otherwise} \end{cases}. \tag{39}$$

Then a DC bias is added in the TD, which is defined as $10\log_{10}(\eta_{\text{DC}}+1)$ dB, where the DC power in the linear domain is given by $\eta_{\text{DC}}\sqrt{E(|s[n, m]|^2)}$. The second major benchmark is DCO-OTFS [52], [53], which modulates QAM symbols in the DD-domain as follows:

$$\widetilde{s}[k, l] = \begin{cases} \widetilde{s}[k, l], & 1 \leq k \leq \frac{N}{2} - 1 \\ \widetilde{s}^*[N - k, l], & \frac{N}{2} + 1 \leq k \leq N - 1 \\ 0, & \text{otherwise} \end{cases}, \tag{40}$$

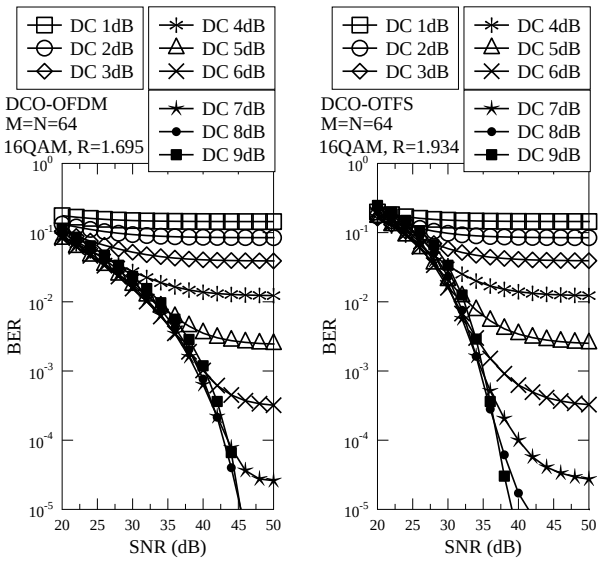

(a) DCO-OFDM (b) DCO-OTFS

Fig. 2: The effect of DC bias of DCO-OFDM and DCO-OTFS associated with $M = N = 64$ using 16QAM.

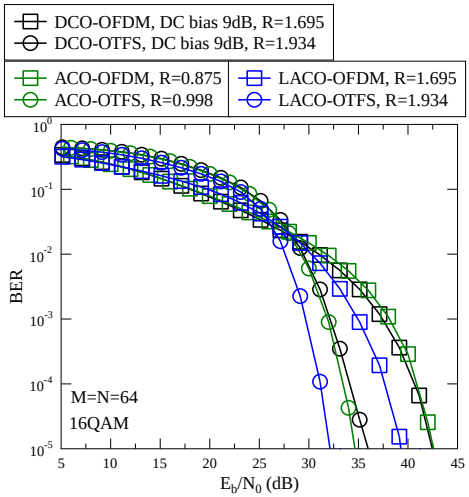

Fig. 3: BER comparison between the O-OTFS schemes of DCO-OTFS, ACO-OTFS and LACO-OTFS as well as the O-OFDM schemes of DCO-OFDM, ACO-OFDM and LACO-OFDM associated with $M = N = 64$ using 16QAM.

and a DC bias is also added in the TD. Thirdly, similar to the proposed LACO-OTFS of (1), the classic LACO-OFDM [7] modulates QAM symbols in the FD as:

$$\overline{s}_j[n,\overline{m}] = \begin{cases} x_j[n,\overline{d}], & \overline{m} = 2^j\overline{d} + 2^{j-1} = \frac{M}{M_j}(2\overline{d}+1) \\ x_j^*[n,\overline{d}], & \overline{m} = M - (2^j\overline{d} + 2^{j-1}) \\ & \quad = \frac{M}{M_j}\left[M_j - (2\overline{d}+1)\right] \\ 0, & \text{otherwise} \end{cases}, \tag{41}$$

where we have $M_j = \frac{M}{2^{j-1}}$ and $0 \leq \overline{d} \leq \frac{M_j}{4} - 1$, and the parameter ranges are given by $1 \leq j \leq J$, $0 \leq n \leq N-1$ and $0 \leq \overline{m} \leq M$. Finally, ACO-OFDM [4] and ACO-OTFS are special cases of LACO-OFDM and LACO-OTFS, respectively, associated with $J = 1$.

Based on the channel model in Sec. II-F, the optical wireless channel is assumed to have $P = 4$, $\tau_{\text{RMS}} = 14$ ns and $K = 0$dB. A CP length of 8 is assumed. Furthermore, the dimensions of $M = N = 64$ and the subcarrier spacing of $\Delta f = 240$ kHz are used in our simulations.

B. The Effect of DC Bias

Fig. 2 portrays the effect of DC bias on both DCO-OFDM and DCO-OTFS, where a sufficient DC bias of up to 9 dB is required to avoid an error floor. This verifies the motivation of LACO-OFDM and LACO-OTFS, which aim for eliminating the DC power consumption, while retaining the full IM/DD throughput. Moreover, Fig. 2 also indicates a throughput difference between O-OFDM and O-OTFS. For an O-OTFS frame size of $N = 64$, its CP overhead is 64 times lower than that of O-OFDM, which requires a separate CP for each symbol. Considering an optical multi-carrier system that has $M = 64$ subcarriers and a subcarrier spacing of $\Delta f = 240$ kHz, the throughputs of $R = 1.695$ bit/sec/Hz and $R = 1.934$ bit/sec/Hz for O-OFDM and O-OTFS lead to the data rates of 26.04 M bit/s and 29.71 M bit/s, respectively. This significant difference in data rate between O-OFDM and O-OTFS will be further increased upon adopting the numerologies of the operational Wi-Fi 6 and 5G New Radio [23], where up to 2048 and 4096 subcarriers can be used, respectively.

C. BER Performance Comparison Between O-OFDM and O-OTFS

Fig. 3 portrays our BER performance comparison between the various O-OFDM and O-OTFS schemes. First of all, the O-OTFS schemes of DCO-OTFS, ACO-OTFS and LACO-OTFS achieve better BER performance and higher throughputs than their O-OFDM counterparts of DCO-OFDM, ACO-OFDM and LACO-OFDM, respectively, as evidenced by Fig. 3. The improved BER performance of the O-OTFS schemes is due to the ISFFT spreading, while the higher throughput is a benefit of using frame-based CP. This confirms the improved bandwidth-efficiency and power-efficiency of O-OTFS over O-OFDM. Secondly, Fig. 3 demonstrates that ACO-OTFS eliminates the DC bias at the cost of a reduced throughput relative to DCO-OTFS, but LACO-OTFS becomes capable of achieving both the same throughput as DCO-OTFS and also the best BER performance, thanks to both the ISFFT spreading and the elimination of DC power consumption.

D. PAPR Comparison Between O-OFDM and O-OTFS

Fig. 4 portrays our comparison between LACO-OFDM and LACO-OTFS in terms of the energy-efficiency of PAPR cumulative distribution function (CCDF). It can be seen in Fig. 4 that the PAPR of LACO-OTFS associated with $N = 4$ is substantially lower than that of its LACO-OFDM counterpart, despite the fact that both schemes have the same $M = 64$ subcarriers. Nonetheless, it is practically favourable to increase the LACO-OTFS frame length to $N = 16$ and $N = 64$ for the sake of a reducing the CP percentage and hence increasing the throughput, which however leads to an increased PAPR that becomes comparable to the LACO-OFDM scheme's PAPR, as evidenced by Fig. 4. This inherent trade-off between bandwidth-efficiency and power-efficiency of O-OTFS may be mitigated by the proposed DFT-S technique, where DFT-S-LACO-OTFS associated with $M = N = 64$ using 4PAM is

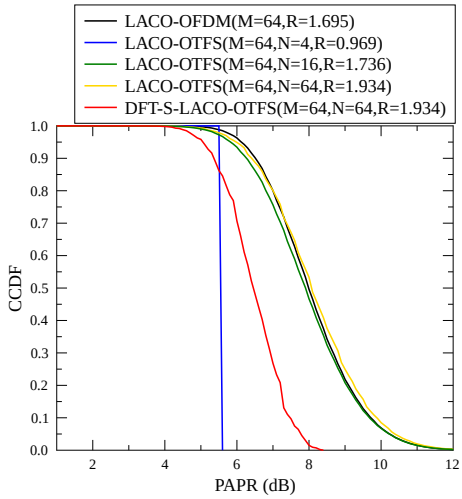

Fig. 4: PAPR comparison between LACO-OFDM and LACO-OTFS associated with $M = 64$ using 16QAM.

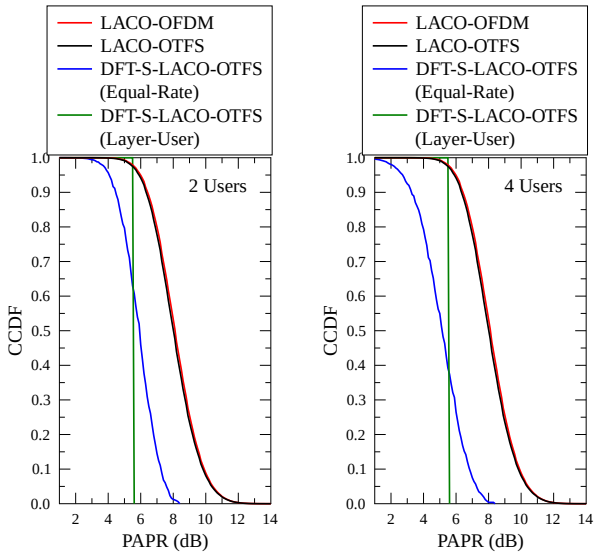

(a) 2 users (b) 4 users

Fig. 5: The effect of DFT-S on PAPR for LACO-OTFS associated with $M = N = 64$.

capable of achieving the same throughput as LACO-OTFS at a substantially reduced PAPR, as evidenced by Fig. 4.

E. PAPR Comparison Between DFT-S-LACO-OTFS Schemes

Fig. 5 demonstrates the effect of DFT-S on the PAPR of LACO-OTFS. First of all, it can be seen in Fig. 5 that both the DFT-S-LACO-OTFS arrangements of Equal-Rate and Layer-User are capable of substantially reducing the multi-carrier PAPRs of LACO-OFDM and LACO-OTFS. Secondly, Fig. 5 demonstrates that the Layer-User method of DFT-S-LACO-OTFS exhibits a better PAPR than the Equal-Rate method. Explicitly, the PAPR of the Layer-User method does not exceed 6 dB.

F. BER Performance of DFT-S-LACO-OTFS Schemes

Fig. 6 portrays our BER comparison between our multi-access techniques. For LACO-OFDM and LACO-OTFS, multi-access is facilitated by dividing the FD subcarriers and DD symbols, respectively, equally amongst the users. For

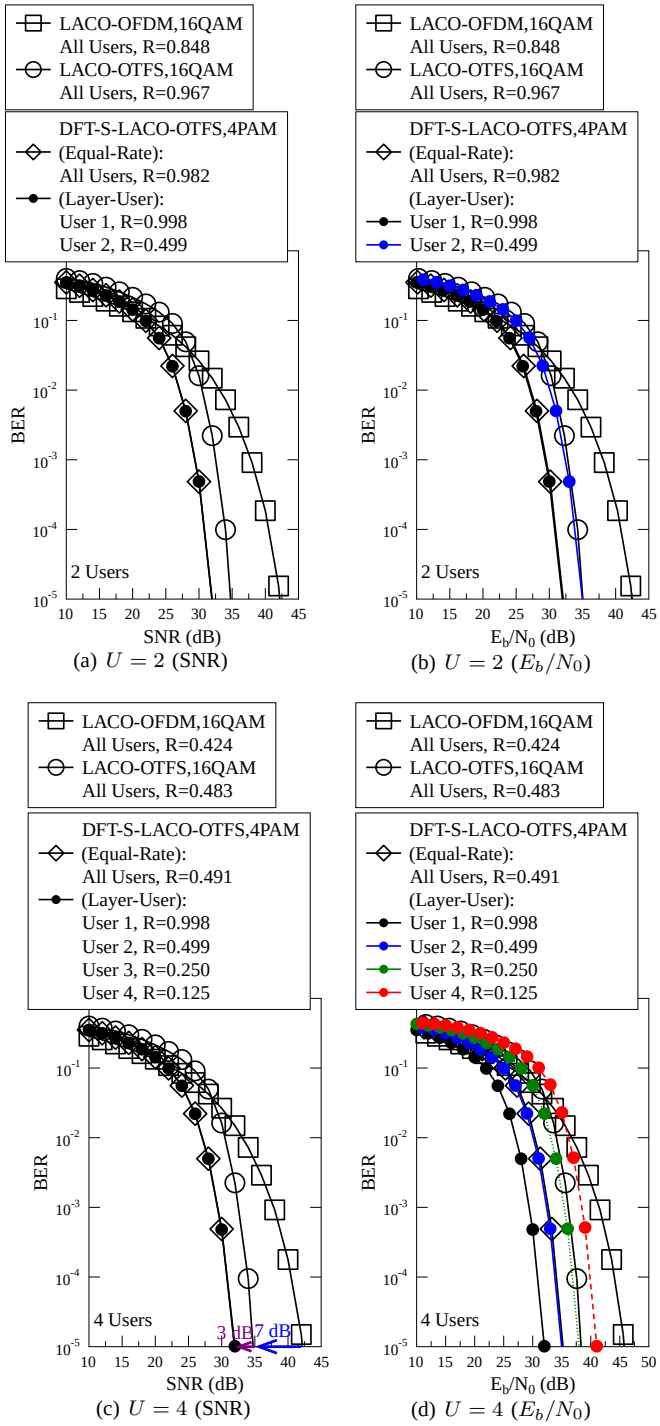

(a) $U = 2$ (SNR) (b) $U = 2$ (E_b/N_0)

(c) $U = 4$ (SNR) (d) $U = 4$ (E_b/N_0)

Fig. 6: BER performance comparison between LACO-OTFS using 16QAM and DFT-S-OTFS using 4PAM.

DFT-S-LACO-OTFS, the multi-access arrangements of Equal-Rate and Layer-User are conceived in Sec. III-B. Observe in Fig. 6 that first of all, LACO-OTFS outperforms LACO-OFDM, benefiting from its ISFFT spreading. Furthermore, DFT-S-LACO-OTFS is capable of achieving a further improved performance over LACO-OTFS, thanks to the benefit of DFT spreading in the DD-domain. Specifically, Fig. 6(c) demonstrates that for a 4-user optical wireless system, LACO-OTFS is capable of achieving a 7 dB SNR gain over LACO-OFDM at BER=10^{-5}, while DFT-S-OTFS is capable of providing a further 3 dB SNR gain over LACO-OTFS.

Secondly, Fig. 6(a) demonstrates that both the Equal-Rate and Layer-User arrangements achieve the same BER performance versus SNR, but the second user of the Layer-User scheme has a worse BER versus E_b/N_0 performance in Fig. 6(b). Similarly, for the case of having $U = 4$ users, both the Equal-Rate and Layer-User arrangements achieve the same BER versus SNR performance in Fig. 6(c), but the second, third and fourth users of the Layer-User scheme exhibit gradually degraded BER versus E_b/N_0 performance in Fig. 6(d). This is due to the fact that the Layer-User arrangement assigns different layers to different users, where the higher layers have decreasing throughputs, as indicated in the legend of Fig. 6.

G. Comparison Between DFT-S-OFDM and DFT-S-LACO-OTFS

Furthermore, although the conventional optical DFT-S-OFDM schemes [28]–[30] did not facilitate multi-access, we apply the Equal-Rate and Layer-User arrangements of (31) and (32) to DFT-S-LACO-OFDM for a fair comparison. For Equal-Rate, a total of $\frac{M_j}{2}$ PAM symbols are equally assigned to U users on each layer before DFT-S in the TF-domain as follows:

$$\check{s}_j[n,\check{d}] = \begin{cases} x_j[n,d], & \check{d} = u\frac{M_j}{2U} + d \\ -x_j[n,d], & \check{d} = u\frac{M_j}{2U} + d + \frac{M_j}{2} \\ 0, & \text{otherwise} \end{cases}, \quad (42)$$

where we have $0 \le d \le \frac{M_j}{2U} - 1$ and $0 \le \check{d} \le M_j - 1$. Similarly, the Layer-User arrangement assigns one layer of $\frac{M_j}{2}$ PAM symbols to one user as follows:

$$\check{s}_j[n,\check{d}] = \begin{cases} x_j[n,d], & \check{d} = d \\ -x_j[n,d], & \check{d} = d + \frac{M_j}{2} \\ 0, & \text{otherwise} \end{cases}, \quad (43)$$

where we have $0 \le d \le \frac{M_j}{2} - 1$ and $0 \le \check{d} \le M_j - 1$. The parameters of DFT-S-LACO-OFDM can be obtained by replacing N and $N_j = \frac{N}{2^{j-1}}$ of DFT-S-LACO-OTFS summarized in Table III by M and $M_j = \frac{M}{2^{j-1}}$, respectively. The M_j-point DFT for each layer $\check{s}_j[n,\check{\overline{m}}] = \frac{1}{\sqrt{M_j}} \sum_{\check{d}=0}^{M_j-1} \check{s}_j[n,\check{d}]\omega_{M_j}^{-\check{d}\check{\overline{m}}}$ leads to:

$$\begin{aligned} &\check{s}_j[n,\check{\overline{m}}] \\ &= \frac{1}{\sqrt{M_j}} \sum_{\check{d}=0}^{\frac{M_j}{2}-1} \left\{ \check{s}_j[n,\check{d}]\omega_{M_j}^{-\check{d}\check{\overline{m}}} + \check{s}_j[n,\check{d}+\tfrac{M_j}{2}]\omega_{M_j}^{-\check{d}\check{\overline{m}}}(\omega_{M_j}^{-\frac{M_j}{2}})^{\check{\overline{m}}} \right\} \\ &= \begin{cases} \frac{2}{\sqrt{M_j}} \sum_{\check{d}=0}^{\frac{M_j}{2}-1} \check{s}_j[n,\check{d}]\omega_{M_j}^{-\check{d}\check{\overline{m}}}, & \check{\overline{m}} \text{ is odd}, \\ 0, & \text{otherwise}, \end{cases} \end{aligned} \quad (44)$$

where $\check{s}_j[n,\check{d}+\frac{M_j}{2}] = -\check{s}_j[n,\check{d}]$ based on (42) and (43) and we have $\omega_{M_j}^{-\frac{M_j}{2}} = -1$. Following this, the subcarrier mapping in the FD is given by:

$$\overline{s}_j[n,\overline{m}] = \begin{cases} \check{s}_j[n,\check{\overline{m}}], & \overline{m} = \frac{M}{M_j}\check{\overline{m}} \\ 0, & \text{otherwise} \end{cases}, \quad (45)$$

which is in the same form as the LACO-OFDM of (41) associated with $\check{\overline{m}} = 2\overline{d}+1$ as well as $\overline{s}_j[n,M-\overline{m}] = \check{\overline{s}}_j[n,M_j-\check{\overline{m}}] = \frac{1}{\sqrt{M_j}} \sum_{\check{d}=0}^{M_j-1} \check{s}_j[n,\check{d}]\omega_{M_j}^{-\check{d}(M_j-\check{\overline{m}})} = \check{\overline{s}}_j^*[n,\check{\overline{m}}] = \overline{s}_j^*[n,\overline{m}]$.

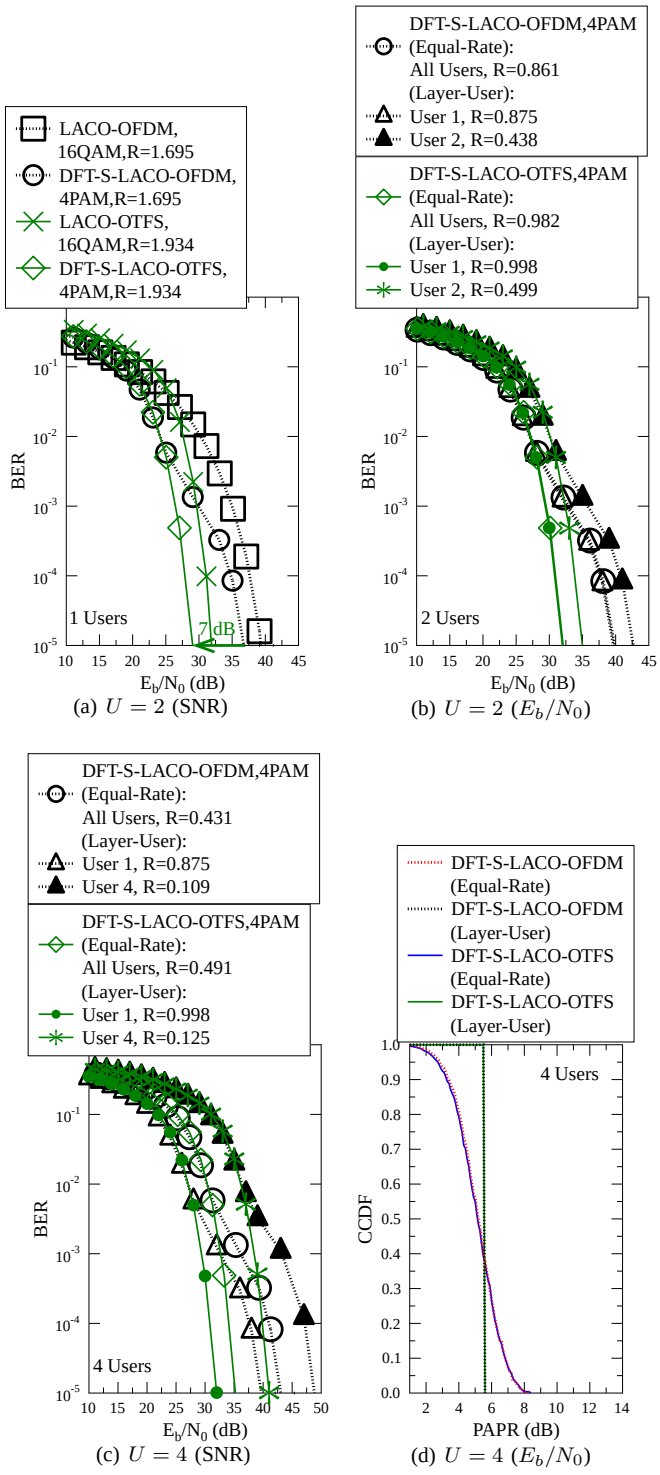

Fig. 7: BER and PAPR comparison between DFT-S-OFDM and DFT-S-OTFS using 4PAM.

Fig. 7 demonstrates the BER and PAPR comparisons between LACO-OFDM and LACO-OTFS schemes. First of all, Fig. 7(a) confirms once again that the proposed LACO-OTFS with and without DFT-S outperform their LACO-OFDM counterparts, where DFT-S-LACO-OTFS is capable of achieving a 7 dB SNR gain over DFT-S-LACO-OFDM at BER=10^{-5}. This is expected because the spreading gain of DFT-S-LACO-OFDM is achieved by DFT-S along the

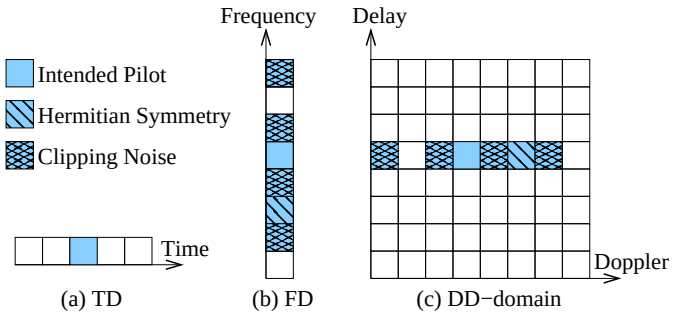

Fig. 8: The effect of Hermitian symmetry and clipping noise on the intended pilot insertion in TD/FD/DD-domains.

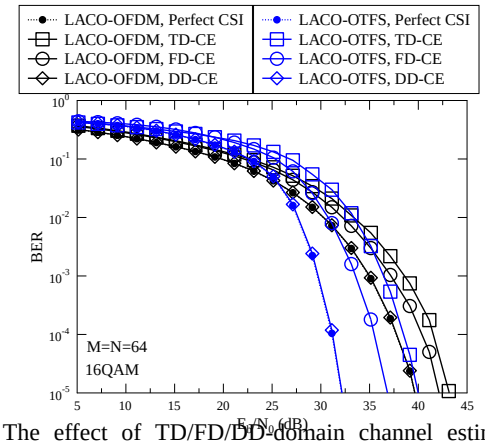

Fig. 9: The effect of TD/FD/DD-domain channel estimation for LACO-OFDM and LACO-OTFS associated with $M = 64$ using 16QAM.

frequency axis in the TF-domain, while the spreading gain of DFT-S-LACO-OTFS is achieved by DFT-S together with ISFFT precoding along both delay and Doppler axes in the DD-domain. Secondly, Figs. 7(b) and (c) evidence that DFT-S-LACO-OTFS outperforms DFT-S-LACO-OFDM counterpart in multi-access scenarios, where the Equal-Rate arrangements achieve the same BER for all users, while the Layer-User arrangements exhibit degraded BER versus E_b/N_0 for users assigned to higher layers. Finally, Fig. 7(d) confirms that both DFT-S-LACO-OTFS and DFT-S-LACO-OFDM exhibit single-carrier PAPR performance.

H. The Effect of Channel Estimation

Finally, regardless of which domain the information is modulated in (i.e. O-OFDM/O-OTFS with/without DFT-S), the optical channel can be estimated in the TD, FD and DD-domain, and then the effect of frequency selectivity is equalized in the FD. However, the requirement of Hermitian symmetry and the clipping noise would contaminate the FD and DD-domain pilot design, as portrayed by Fig. 8. More explicitly, firstly, the TD channel estimation is facilitated by inserting a Dirac delta impulse-based CP in the TD, as portrayed by Fig. 8(a). Following the TD convolution between the impulse-based pilot CP and the CIRs modelled in Sec. II-F, the CIRs are estimated one by one without interference. This is not affected by clipping as the TD pilot can be directly modulated to be a unipolar symbol. Secondly, the conventional FD channel estimation aims for inserting pilots periodically in the FD as $\overline{m}' \in \{0, \mathcal{N}_{PS}^{FD}, 2\mathcal{N}_{PS}^{FD}, \cdots, (\mathcal{N}_p^{FD}-1)\mathcal{N}_{PS}^{FD}\}$, where $\mathcal{N}_{PS}^{FD}$ refers to the pilot spacing in the FD [39], [63], [64]. However, as shown by Fig. 8(b), this periodicity is no longer sustainable for O-OFDM and O-OTFS schemes owing to the requirement of Hermitian symmetry and due to the FD spreading induced by clipping noise. Similarly, the conventional DD-domain channel estimation [37]–[39] relies on a Dirac delta impulse-based pilot design in the DD-domain, which is also contaminated by Hermitian symmetry and clipping noise, as shown by Fig. 8(c). For this reason, for the FD and DD-domain channel estimation, we propose to fully modulate all symbols in an O-OFDM symbol and an O-OTFS frame, respectively, as pilots for channel estimation. The pilot symbols are known at the receiver, hence the FDE is capable of recovering the channel's frequency responses at all subcarriers, and the DD-domain fading can be recovered via SFFT. Given the quasi-static nature of optical channels, the pilot overhead is negligible, since the pilots do not have to be repeated.

Fig. 9 demonstrates the effect of TD/FD/DD-domain channel estimation. We note that the pilot overheads of TD/FD/DD-domain channel estimation are given by a CP, an O-OFDM symbol and an O-OTFS frame. As a result, the DD-domain channel estimation performs the best at the cost of the highest pilot overhead, followed by the FD and TD channel estimation techniques, as evidenced by Fig. 9.

I. The Effect of Channel Dispersion

Finally, the effect of channel dispersion is portrayed in Fig. 10, where the single-carrier on-off keying (OOK) [65] and multi-carrier LACO-OFDM as well as the proposed LACO-OTFS schemes are compared. Figs. 10(a)-(d) demonstrate that for the case of $P = 1$ CIR tap corresponding to no dispersion, LACO-OFDM and LACO-OTFS cannot achieve any performance gains, despite their increased complexity imposed by the FFT/IFFT operations. However, Fig. 10(a) demonstrates that for the Ricean factor of K=3 dB and $P = 2$ CIR taps, the proposed LACO-OTFS performs the best, followed by LACO-OFDM, while the single-carrier OOK exhibits an irreducible error floor. The performance differences between the three schemes are gradually reduced for $P = 2$, when the Ricean K factor is increased to 6 dB, 9 dB and 12 dB in Figs. 10(b)-(d). Nonetheless, we note that first of all, the OOK performance results of Fig. 10 assume perfect CSI, which in reality still has to rely on the proposed TD/FD/DD channel estimation techniques shown in Sec. IV-H. Secondly, even when the slightest dispersion emerges for $P = 2$ associated with the maximum delay of $\tau_{\max} = 16$ ns, the OOK performance is severely degraded by the ISI, as evidenced by Fig. 10.

V. Conclusions

We demonstrate that the proposed LACO-OTFS is capable of improving the bandwidth-/power-/energy-efficiency of the existing O-OFDM and O-OTFS schemes. In order to ensure as low a PAPR as single-carrier transmission and a low CP percentage, we proposed DFT-S-LACO-OTFS that performs DFT based spreading in the DD-domain. A pair of multi-access arrangements have also been conceived. We explicitly demonstrated that regardless of which domain the information

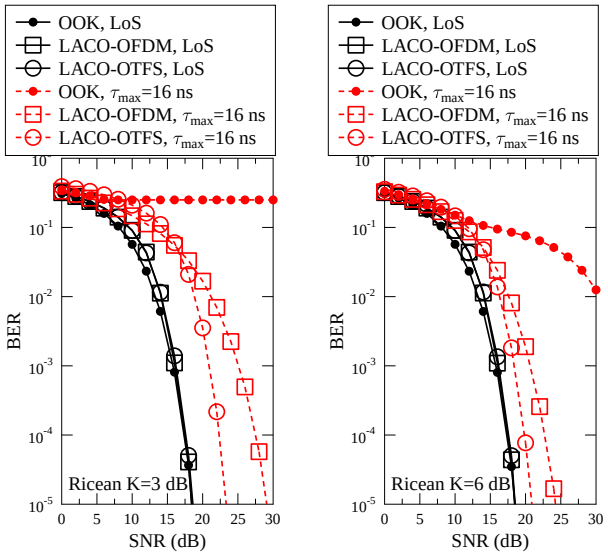

(a) Ricean K=3 dB (b) Ricean K=6 dB

(c) Ricean K=9 dB (d) Ricean K=12 dB

Fig. 10: The effect of channel dispersion for single-carrier on-off keying (OOK) and multi-carrier LACO-OFDM (using 4QAM) as well as the proposed LACO-OTFS (using 4QAM), where we have $M = 256$, $N = 64$ and $\Delta f = 240$ kHz. The cases of $P = 1$ CIR and $P = 2$ CIRs correspond to the maximum delays of $\tau_{\max} = 0$ ns and $\tau_{\max} = 16$ ns, respectively.

is modulated in (i.e. O-OFDM/O-OTFS with/without DFT-S), the quasi-static optical channel can be estimated in the TD/FD/DD-domain and then equalized in the FD. As a benefit, the computational complex MMSE and MP detectors routinely used in RF-OTFS are avoided for our O-OTFS schemes. Our simulation results confirm the advantages of O-OTFS over O-OFDM in terms of its throughput (bandwidth-efficiency), BER (power-efficiency) and PAPR (energy-efficiency). This is achieved at the extra cost of ISFFT/SFFT. Nonetheless, as presented in Fig. 1, the transformation between DD and TD implemented by the ISFFT followed by a IDFT is equivalent to a single-step IDFT. The full ISFFT/SFFT is only needed for FDE, when the transformation between DD and FD is required. Moreover, the DD-domain channel estimation technique is shown to perform better than its FD and TD counterparts, albeit at the cost of a higher pilot overhead.

REFERENCES

[1] J. Armstrong, "OFDM for optical communications," *J. Lightw. Technol.*, vol. 27, no. 3, pp. 189–204, 2009.

[2] S. Dissanayake and J. Armstrong, "Comparison of ACO-OFDM, DCO-OFDM and ADO-OFDM in IM/DD systems," *J. Lightw. Technol.*, vol. 31, no. 7, pp. 1063–1072, 2013.

[3] X. Zhang, Z. Babar, P. Petropoulos, H. Haas, and L. Hanzo, "The evolution of optical OFDM," *IEEE Commun. Surveys Tuts.*, vol. 23, no. 3, pp. 1430–1457, 2021.

[4] J. Armstrong and A. Lowery, "Power efficient optical OFDM," *Electron. Lett.*, vol. 42, no. 6, pp. 370–372, 2006.

[5] S. Lee, S. Randel, F. Breyer, and A. Koonen, "PAM-DMT for intensity-modulated and direct-detection optical communication systems," *IEEE Photonics Technol. Lett.*, vol. 21, no. 23, pp. 1749–1751, 2009.

[6] N. Fernando, Y. Hong, and E. Viterbo, "Flip-OFDM for unipolar communication systems," *IEEE Trans. Commun.*, vol. 60, no. 12, pp. 3726–3733, 2012.

[7] Q. Wang, C. Qian, X. Guo, Z. Wang, D. G. Cunningham, and H. H. White, "Layered ACO-OFDM for intensity-modulated direct-detection optical wireless transmission," *Opt. Express*, vol. 23, no. 9, pp. 12382–12393, 2015.

[8] X. Liu, J. Zhou, N. Huang, and W. Zhang, "Improved receivers for optical wireless OFDM: An information theoretic perspective," *IEEE Trans. Commun.*, vol. 70, no. 7, pp. 4439–4453, 2022.

[9] S. Zhang, S. Watson, J. McKendry, D. Massoubre, A. Cogman, E. Gu, R. Henderson, A. Kelly, and M. Dawson, "1.5 Gbit/s multi-channel visible light communications using CMOS-controlled GaN-based LEDs," *J. Lightw. Technol.*, vol. 31, no. 8, pp. 1211–1216, 2013.

[10] J. Kahn and J. Barry, "Wireless infrared communications," *Proc. IEEE*, vol. 85, no. 2, pp. 265–298, 1997.

[11] F. Miramirkhani and M. Uysal, "Channel modeling and characterization for visible light communications," *IEEE Photonics J.*, vol. 7, no. 6, pp. 1–16, 2015.

[12] M. Uysal, F. Miramirkhani, O. Narmanlioglu, T. Baykas, and E. Panayirci, "IEEE 802.15.7r1 reference channel models for visible light communications," *IEEE Commun. Mag.*, vol. 55, no. 1, pp. 212–217, 2017.

[13] M. Mossaad, S. Hranilovic, and L. Lampe, "Visible light communications using OFDM and multiple LEDs," *IEEE Trans. Commun.*, vol. 63, no. 11, pp. 4304–4313, 2015.

[14] J. Carruthers and J. Kahn, "Multiple-subcarrier modulation for nondirected wireless infrared communication," *IEEE J. Sel. Areas Commun.*, vol. 14, no. 3, pp. 538–546, 1996.

[15] J. Carruthers and J. Kahn, "Modeling of nondirected wireless infrared channels," *IEEE Trans. Commun.*, vol. 45, no. 10, pp. 1260–1268, 1997.

[16] V. Jungnickel, V. Pohl, S. Nonnig, and C. von Helmolt, "A physical model of the wireless infrared communication channel," *IEEE J. Sel. Areas Commun.*, vol. 20, no. 3, pp. 631–640, 2002.

[17] D. N. Amanor, W. W. Edmonson, and F. Afghah, "Intersatellite communication system based on visible light," *IEEE Trans. Aerosp. Electronic Syst.*, vol. 54, no. 6, pp. 2888–2899, 2018.

[18] Q. Yang, L. Tan, and J. Ma, "Doppler characterization of laser intersatellite links for optical LEO satellite constellations," *Optics Commun.*, vol. 282, no. 17, pp. 3547–3552, 2009.

[19] H. Sun, Q. Liu, J. Wang, J. Ren, Y. Wu, H. Zhao, and H. Li, "Fusion of infrared and visible images for remote detection of low-altitude slow-speed small targets," *IEEE J. Sel. Topics Applied Earth Observations and Remote Sensing*, vol. 14, pp. 2971–2983, 2021.

[20] B. G. Guzman, V. P. G. Jimenez, M. C. Aguayo-Torres, H. Haas, and L. Hanzo, "Downlink performance of optical OFDM in outdoor visible light communication," *IEEE Access*, vol. 6, pp. 76854–76866, 2018.

[21] C. Xu, J. Zhang, T. Bai, P. Botsinis, R. G. Maunder, R. Zhang, and L. Hanzo, "Adaptive coherent/non-coherent single/multiple-antenna aided channel coded ground-to-air aeronautical communication," *IEEE Trans. Commun.*, vol. 67, no. 2, pp. 1099–1116, 2019.

[22] C. Xu, T. Bai, J. Zhang, R. Rajashekar, R. G. Maunder, Z. Wang, and L. Hanzo, "Adaptive coherent/non-coherent spatial modulation aided unmanned aircraft systems," *IEEE Wireless Commun.*, vol. 26, no. 4, pp. 170–177, 2019.

[23] C. Xu, N. Ishikawa, R. Rajashekar, S. Sugiura, R. G. Maunder, Z. Wang, L. Yang, and L. Hanzo, "Sixty years of coherent versus non-coherent tradeoffs and the road from 5G to wireless futures," *IEEE Access*, vol. 7, pp. 178246–178299, 2019.

[24] X. Li, J. Vucic, V. Jungnickel, and J. Armstrong, "On the capacity of intensity-modulated direct-detection systems and the information rate

of ACO-OFDM for indoor optical wireless applications," *IEEE Trans. Commun.*, vol. 60, no. 3, pp. 799–809, 2012.
[25] X. Zhang, Q. Wang, R. Zhang, S. Chen, and L. Hanzo, "Performance analysis of layered ACO-OFDM," *IEEE Access*, vol. 5, pp. 18366–18381, 2017.
[26] X. Zhang, Z. Babar, R. Zhang, S. Chen, and L. Hanzo, "Multi-class coded layered asymmetrically clipped optical OFDM," *IEEE Trans. Commun.*, vol. 67, no. 1, pp. 578–589, 2019.
[27] R. Bai and S. Hranilovic, "Absolute value layered ACO-OFDM for intensity-modulated optical wireless channels," *IEEE Trans. Commun.*, vol. 68, no. 11, pp. 7098–7110, 2020.
[28] O. Saied, X. Li, and K. M. Rabie, "DFT spread-optical pulse amplitude modulation for visible light communication systems," *IEEE Access*, vol. 10, pp. 15956–15967, 2022.
[29] J. Zhou, Z. Zhang, T. Zhang, M. Guo, X. Tang, and Z. Wang, "A combined PAPR-reduction technique for asymmetrically clipped optical OFDM system," *Optics Commun.*, vol. 366, pp. 451–456, 2016.
[30] R. Bai, Z. Wang, R. Jiang, and J. Cheng, "Interleaved DFT-spread layered/enhanced ACO-OFDM for intensity-modulated direct-detection systems," *J. Lightwave Technol.*, vol. 36, no. 20, pp. 4713–4722, 2018.
[31] H. G. Myung, J. Lim, and D. J. Goodman, "Single carrier FDMA for uplink wireless transmission," *IEEE Veh. Technol. Mag.*, vol. 1, pp. 30–38, Sep. 2006.
[32] N. Benvenuto, R. Dinis, D. Falconer, and S. Tomasin, "Single carrier modulation with nonlinear frequency domain equalization: An idea whose time has comeagain," *Proc. IEEE*, vol. 98, pp. 69–96, Jan 2010.
[33] C. Xu, Y. Xiong, N. Ishikawa, R. Rajashekar, S. Sugiura, Z. Wang, S. X. Ng, L.-L. Yang, and L. Hanzo, "Space-, time- and frequency-domain index modulation for next-generation wireless: A unified single-/multi-carrier and single-/multi-RF MIMO framework," *IEEE Trans. Wireless Commun.*, vol. 20, no. 6, pp. 3847–3864, 2021.
[34] R. Hadani, S. Rakib, M. Tsatsanis, A. Monk, A. Goldsmith, A. Molisch, and R. Calderbank, "Orthogonal time frequency space modulation," in *2017 IEEE Wireless Communications and Networking Conference (WCNC)*, pp. 1–6, 2017.
[35] Z. Wei, W. Yuan, S. Li, J. Yuan, G. Bharatula, R. Hadani, and L. Hanzo, "Orthogonal time-frequency space modulation: A promising next-generation waveform," *IEEE Wireless Commun.*, vol. 28, no. 4, pp. 136–144, 2021.
[36] S. Mohammed, "Derivation of OTFS modulation from first principles," *IEEE Trans. Veh. Technol.*, vol. 70, no. 8, pp. 7619–7636, 2021.
[37] P. Raviteja, K. T. Phan, and Y. Hong, "Embedded pilot-aided channel estimation for OTFS in delaydoppler channels," *IEEE Trans. Veh. Technol.*, vol. 68, no. 5, pp. 4906–4917, 2019.
[38] W. Shen, L. Dai, J. An, P. Fan, and R. Heath, "Channel estimation for orthogonal time frequency space (OTFS) massive MIMO," *IEEE Trans. Signal Process.*, vol. 67, no. 16, pp. 4204–4217, 2019.
[39] C. Xu, L. Xiang, J. An, C. Dong, S. Sugiura, R. G. Maunder, L.-L. Yang, and L. Hanzo, "OTFS-aided RIS-assisted SAGIN systems outperform their OFDM counterparts in doubly selective high-doppler scenarios," *IEEE Internet Things J.*, vol. 10, no. 1, pp. 682–703, 2023.
[40] A. Farhang, A. RezazadehReyhani, L. Doyle, and B. Farhang-Boroujeny, "Low complexity modem structure for OFDM-based orthogonal time frequency space modulation," *IEEE Wireless Commun. Lett.*, vol. 7, no. 3, pp. 344–347, 2018.
[41] P. Raviteja, Y. Hong, E. Viterbo, and E. Biglieri, "Practical pulse-shaping waveforms for reduced-cyclic-prefix OTFS," *IEEE Trans. Veh. Technol.*, vol. 68, no. 1, pp. 957–961, 2019.
[42] Z. Wei, W. Yuan, S. Li, J. Yuan, and D. Ng, "Transmitter and receiver window designs for orthogonal time-frequency space modulation," *IEEE Trans. Commun.*, vol. 69, no. 4, pp. 2207–2223, 2021.
[43] G. Surabhi, R. Augustine, and A. Chockalingam, "On the diversity of uncoded OTFS modulation in doubly-dispersive channels," *IEEE Trans. Wireless Commun.*, vol. 18, no. 6, pp. 3049–3063, 2019.
[44] P. Raviteja, Y. Hong, E. Viterbo, and E. Biglieri, "Effective diversity of OTFS modulation," *IEEE Wireless Commun. Lett.*, vol. 9, no. 2, pp. 249–253, 2020.
[45] S. Li, J. Yuan, W. Yuan, Z. Wei, B. Bai, and D. Ng, "Performance analysis of coded OTFS systems over high-mobility channels," *IEEE Trans. Wireless Commun.*, vol. 20, no. 9, pp. 6033–6048, 2021.
[46] P. Raviteja, E. Viterbo, and Y. Hong, "OTFS performance on static multipath channels," *IEEE Wireless Commun. Letts.*, vol. 8, no. 3, pp. 745–748, 2019.
[47] S. Tiwari, S. Das, and V. Rangamgari, "Low complexity LMMSE receiver for OTFS," *IEEE Commun. Lett.*, vol. 23, no. 12, pp. 2205–2209, 2019.
[48] G. Surabhi and A. Chockalingam, "Low-complexity linear equalization for OTFS modulation," *IEEE Commun. Lett.*, vol. 24, no. 2, pp. 330–334, 2020.
[49] P. Raviteja, K. Phan, Y. Hong, and E. Viterbo, "Interference cancellation and iterative detection for orthogonal time frequency space modulation," *IEEE Trans. Wireless Commun.*, vol. 17, no. 10, pp. 6501–6515, 2018.
[50] W. Yuan, Z. Wei, J. Yuan, and D. Ng, "A simple variational Bayes detector for orthogonal time frequency space (OTFS) modulation," *IEEE Trans. Veh. Technol.*, vol. 69, no. 7, pp. 7976–7980, 2020.
[51] L. Xiang, Y. Liu, L. Yang, and L. Hanzo, "Gaussian approximate message passing detection of orthogonal time frequency space modulation," *IEEE Trans. Veh. Technol.*, vol. 70, no. 10, pp. 10999–11004, 2021.
[52] J. Zhong, J. Zhou, W. Liu, and J. Qin, "Orthogonal time-frequency multiplexing with 2D hermitian symmetry for optical-wireless communications," *IEEE Photonics J.*, vol. 12, no. 2, pp. 1–10, 2020.
[53] D. Zheng, H. Zhang, and J. Song, "DCO-OTFS-based full-duplex relay-assisted visible light communications," *Opt. Express*, vol. 29, no. 25, pp. 41323–41332, 2021.
[54] T. V. Luong, X. Zhang, L. Xiang, T. M. Hoang, C. Xu, P. Petropoulos, and L. Hanzo, "Deep learning-aided optical IM/DD OFDM approaches the throughput of RF-OFDM," *IEEE J. Sel. Areas Commun.*, vol. 40, no. 1, pp. 212–226, 2022.
[55] X. Zhang, T. V. Luong, P. Petropoulos, and L. Hanzo, "Machine-learning-aided optical OFDM for intensity modulated direct detection," *J. Lightw. Technol.*, vol. 40, no. 8, pp. 2357–2369, 2022.
[56] M. Garrido, "A survey on pipelined FFT hardware architectures," *J. Signal Process. Syst.*, vol. 94, no. 11, pp. 1345–1364, 2022.
[57] R. Steele and L. Hanzo, *Mobile Radio Communications*. John Wiley & Sons, May 1999.
[58] J. G. Proakis, *Digital Communications*. New York: McGraw-Hill, 1995.
[59] A. Goldsmith, *Wireless communications*. Cambridge University Press, 2005.
[60] L. Hanzo, O. Alamri, M. El-Hajjar, and N. Wu, *Near-Capacity Multi-Functional MIMO Systems: Sphere-Packing, Iterative Detection and Cooperation*. John Wiley & Sons, May 2009.
[61] S. Long, M. A. Khalighi, M. Wolf, S. Bourennane, and Z. Ghassemlooy, "Investigating channel frequency selectivity in indoor visible-light communication systems," *IET Optoelectronics*, vol. 10, no. 3, pp. 1751–8768, 2016.
[62] S. Dimitrov, S. Sinanovic, and H. Haas, "Clipping noise in OFDM-based optical wireless communication systems," *IEEE Trans. Commun.*, vol. 60, no. 4, pp. 1072–1081, 2012.
[63] Y. Yang, B. Zheng, S. Zhang, and R. Zhang, "Intelligent reflecting surface meets OFDM: Protocol design and rate maximization," *IEEE Trans. Commun.*, vol. 68, no. 7, pp. 4522–4535, 2020.
[64] C. Xu, J. An, T. Bai, L. Xiang, S. Sugiura, R. Maunder, L. Yang, and L. Hanzo, "Reconfigurable intelligent surface assisted multi-carrier wireless systems for doubly selective high-mobility ricean channels," *IEEE Trans. Veh. Technol.*, vol. 71, no. 4, pp. 4023–4041, 2022.
[65] D. Barros, S. Wilson, and J. Kahn, "Comparison of orthogonal frequency-division multiplexing and pulse-amplitude modulation in indoor optical wireless links," *IEEE Trans. Commun.*, vol. 60, no. 1, pp. 153–163, 2012.